Feasibility of 3D-printed phantoms for quantifying Bragg peak degeneration due to tissue heterogeneity in lung proton therapy

Thijs Moret

Supervised by dr. Eelco Lens

Master thesis performed at:

Medical Physics and Technology

Department of Radiation, Science and Technology

Faculty of Applied Sciences

Delft University of Technology

REACTOR INSTITUTE DELFT

MP&T

Medical Physics & Technology

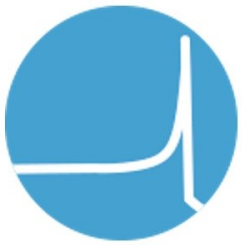

To be examined by:

dr. ir. D.R. Schaart

prof. dr. ir. H. van der Graaf

dr. L. van Eijck

Abstract

In the field of radiation oncology, proton therapy is a relatively new technique. It shows a great advantage over conventional radiation therapy in the depth-dose relation, which results in the possibility to deliver dose far more concentrated at a specific depth. This in turn has the potential to spare the healthy tissue surrounding a tumour from receiving a very high dose. However, this depth-dose relation has the downside that it is very sensitive to small uncertainties in geometry and tissue composition, which are present in heterogeneous tissues such as lung tissue.

Because of this sensitivity, it is essential that the dose delivery can be verified properly for these heterogeneous tissues, which requires highly accurate quality assurance. To improve this quality assurance, highly anthropomorphic phantoms could offer a solution. The currently commercially available phantoms however lack the high level of detail necessary, as these are produced using casting techniques. Thus a new production technique should be considered to create phantoms of greater heterogeneity and at a higher level of detail. A possible solution to this problem is to apply additive manufacturing, since this manufacturing technique can supposedly address both these issues.

An important issue with the application of additive manufacturing is the lack of knowledge on the accuracy of 3D-printers. Next to the unknown accuracy, there are other challenges concerning additive manufacturing, such as the layered creation of objects and the material that is to be printed over an air cavity and the support structures this is associated with.

The goal of this research is to explore the possibility to apply additive manufacturing in the creation of a phantom with a high level of detail and heterogeneity and the effect of the heterogeneous object on the quality of the Bragg peak. More specifically, simulations are performed on porous materials to quantify the degeneration of the Bragg peak. Also, a literature study on additive manufacturing will be performed, combined with the use of commercially available tabletop 3D-printers. Together, the capacity of the printer to create a high level of heterogeneity and the simulations performed on these heterogeneous structures, should give an indication on the feasibility to create a 3D-printed phantom for lung proton therapy.

Table of contents

List of abbreviations

RT – Radiation Therapy
CRT – Conventional Radiation Therapy
LET – Linear Energy Transfer
SOBP – Spread Out Bragg Peak
PBP – Pristine Bragg Peak
QA – Quality Assurance
AM – Additive Manufacturing
CM – Conventional Manufacturing
CAD – Computer Aided Design
STL – Standard Tessellation Language
FDM – Fused Deposition Modelling
MJ – Material Jetting
ME – Material Extrusion
MJM – Multi-jet modelling
PBF – Powder Bed Fusion
BJ – Binder Jetting
VPP – Vat Photopolymerisation
SL – Sheet Lamination
DED – Direct Energy Deposition
UAM – Ultrasonic Additive Manufacturing
-L – AM with a Laser heat source
-EB – AM with an Electron Beam heat source
-PA – AM with a Plasma Arc heat source
-GMA – AM with a Gas Metal Arc heat source
UAM – Ultrasonic Additive Manufacturing
SLA – Stereolithography
SLA-top – Stereolithography illuminated from the top
SLA-bottom – Stereolithography illuminated from the bottom
DLP – Digital Light Processing
LOM – Laminated Object Manufacturing
MC – Monte Carlo
PVA – Polyvinyl Alcohol
SPB – Single Pencil Beam
FW80M – Full width at 80% of the maximum
FWHM – Full width at half maximum

Introduction

In 2018, in The Netherlands alone, over 115000 people were diagnosed with cancer, of whom nearly 45000 passed away due to the disease. [1] The treatment of the disease can be categorised in three main groups, either surgery, chemotherapy or radiation therapy, or a combination of these. Radiation therapy (RT) is where the tumour is irradiated with ionising radiation in order to kill the tumour cells.

Proton therapy is one such type of external radiation therapies. It uses protons to treat the tumour, rather than an X-Ray beam or γ-source, which are used in conventional radiation therapy (CRT). A great advantage of applying proton therapy over CRT, is the possibility to more precisely deliver the dose to the tumour, but not the healthy tissue around it, thus sparing more healthy tissue. This especially is of great importance, when there the tumour is located in close proximity of either a critical organ or an organ which has a higher tissue weighting factor, such as the gonads, oesophagus or thyroid. [2] [3] A more detailed description on proton therapy and how it differs from CRT is presented in the section Proton Therapy.

The potential of proton therapy to combat tumours was already described in 1946 by Robert R. Wilson [4], and has gained in popularity as a viable treatment since then. However, it took until 2018 before this treatment was introduced in The Netherlands. The long duration between the first postulation of the potential of protons and their clinical application can be attributed to three main factors. Firstly, there is a financial barrier, since a proton therapy treatment facility is expensive, secondly the range uncertainties that originate from a combination of imaging, patient setup, beam delivery and dose calculations, both in Quality assurance and in the actual treatment. [5] Lastly, the biological effects of proton radiation is understudied. [6]

The aim of this thesis project is on the feasibility to create a phantom using additive manufacturing that closely resembles tissue heterogeneity in lung tissue, with which to quantify the degeneration of the Bragg peak due to tissue heterogeneity in lung proton therapy.

This requires an understanding of additive manufacturing, for which a literature study is conducted on the potential of this manufacturing technique, which is included in this thesis in the sections Additive Manufacturing and AM processes. The subsequent chapters elaborate on the on the materials and methods for this thesis, such as Monte Carlo simulations, and the results this yields. This also includes the design of porous structures with computer aided design software and the simulations performed on these structures.

Theory

Proton Therapy

Proton therapy is a relatively new technique to combat tumours, in which protons are used to irradiate the tumour, instead of in conventional techniques that use photons to irradiate. As a treatment, the first use of proton therapy for humans was in 1954 at the Lawrence Berkeley Laboratory [7], although the medical benefit of using proton beams was postulated as early as 1946. [4] The first proton therapy facilities were mainly based in research institutes, but this changed in 1990, with the first hospital based proton therapy facility at Loma Linda University Medical Centre. It took some more years before proton therapy treatment systems became commercially available in 2001, and since its commercial introduction, the availability of proton therapy has increased rapidly. [8] The first Dutch proton therapy treatment facility opened in 2018.

The greatest advantage to use protons is shown in Figure 1, the characteristic dose depth profile of protons. If the proton beam is mono-energetic, the dose depth profile will be as the figure shows, with a low entrance dose and a sharp dose fall-off at the tail-end of the proton range, with a sharp, high peak just before the end of the range, called the Bragg peak. [9] This distinct shape of the dose distribution is a result of the way in which protons deposit their energy. They lose energy mainly via electromagnetic interactions with orbital electrons of atoms. This process is inversely proportional to the velocity of the protons, thus meaning that as the protons slow down, the amount of energy that is deposited per unit length, or Linear Energy Transfer (LET), increases along its travelled path. [9]

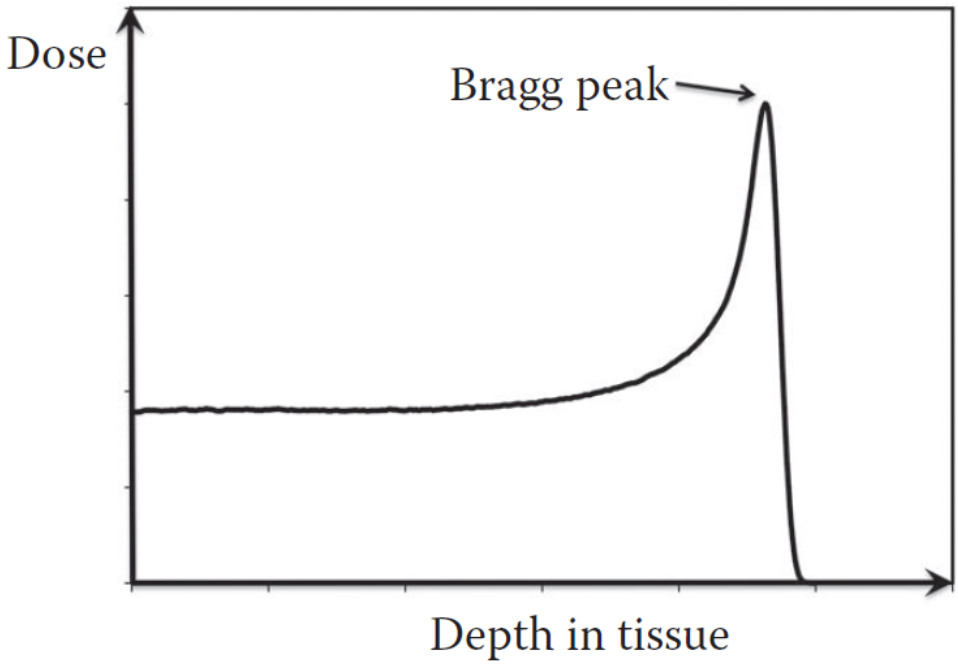

Figure 1, Normalised dose depth distribution for protons as a function of depth, leading to the characteristic Bragg Peak. [9]

This shape of the Bragg peak means that the dose to tissue surrounding the tumour can be irradiated far less than in conventional photon therapy. This is depicted in Figure 2, in which the dose for both photons and protons has been normalised at the tumour location. Also, this graph shows a so called Spread Out Bragg Peak (SOBP), which is a weighted combination of multiple Pristine Bragg Peaks (PBP) with different energies. From the figure it can be clearly seen that there is a significant overdosage both before and after the tumour when using photons instead of protons. The sharp fall-off in dose can be a great asset in the treatment of tumours close to critical organs. [10] This, however, also comes with its own downside: if there is a slight shift in dose distribution, this can cause the tumour to receive far less dose, or even no dose at all, with the Bragg peak ending in healthy tissues. Contrary, a similar shift in photon therapy would result in a very minute dose difference in the tumour.

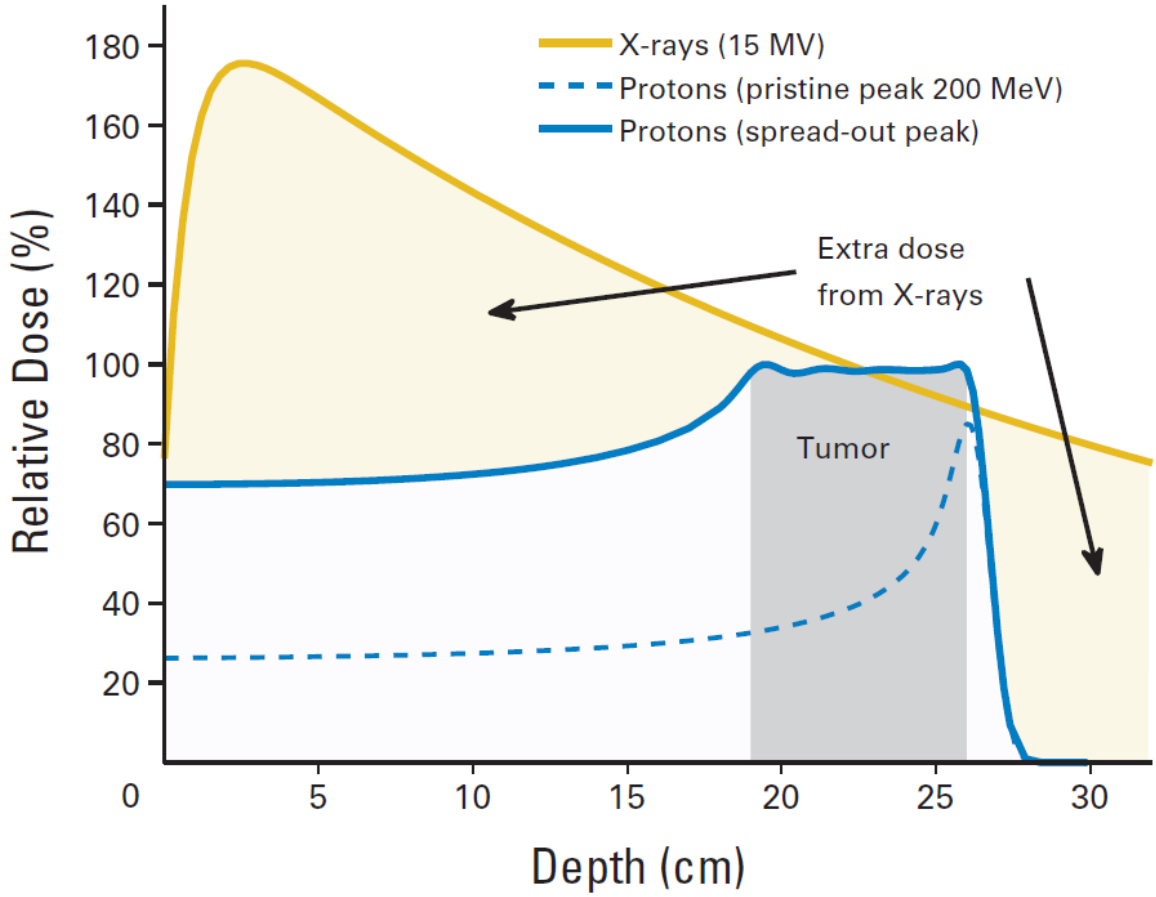

Figure 2, Comparison of normalised dose distributions in a tumour, for photons and protons. [11]

A shift in the Bragg peak location can have a great multitude of origins, but the major source of uncertainty in the correct distribution of dose in the light of this research comes from the heterogeneous nature of tissue. Since the range of protons not only depends on the initial energy of the protons, but also on the material the beam passes through, the heterogeneity of human tissue directly influence where the Bragg peak will end up in the patient. [9] This means that the range is sensitive to both the anatomy of the patient and small geometric changes therein, to a much greater extent than is the case in photon therapy. Therefore it is of great importance that the treatment planning system is able to cope with these inhomogeneities of the body.

To test for this, phantoms are used. With this phantom, the Quality Assurance (QA) for the treatment planning system can be performed, which will give the user a quantitative measure

of the uncertainties in the proton therapy treatment system. In order to achieve maximum effectiveness with these tests, will these be performed with anthropomorphic phantoms to simulate a true patient. These phantoms may include air cavities or bladder-substitutes filled with liquid, bone structures or density gradients in both soft and bone tissue. All together, this results in a phantom with the possibility to a large heterogeneity. However, the currently commercially available phantoms still lack the desired small detail level in geometry, as is shown for selected phantoms in Figure 3. Ideally, a phantom should have the exact same level of detail as the human body, however, this is impossible to obtain with the current production techniques of casting. This results in available phantoms that are barely recognisable as to represent a human, to phantoms that contain actual pieces of human bone. Furthermore, a higher level of detail in the phantom is directly related to a higher price of the phantom. [12]

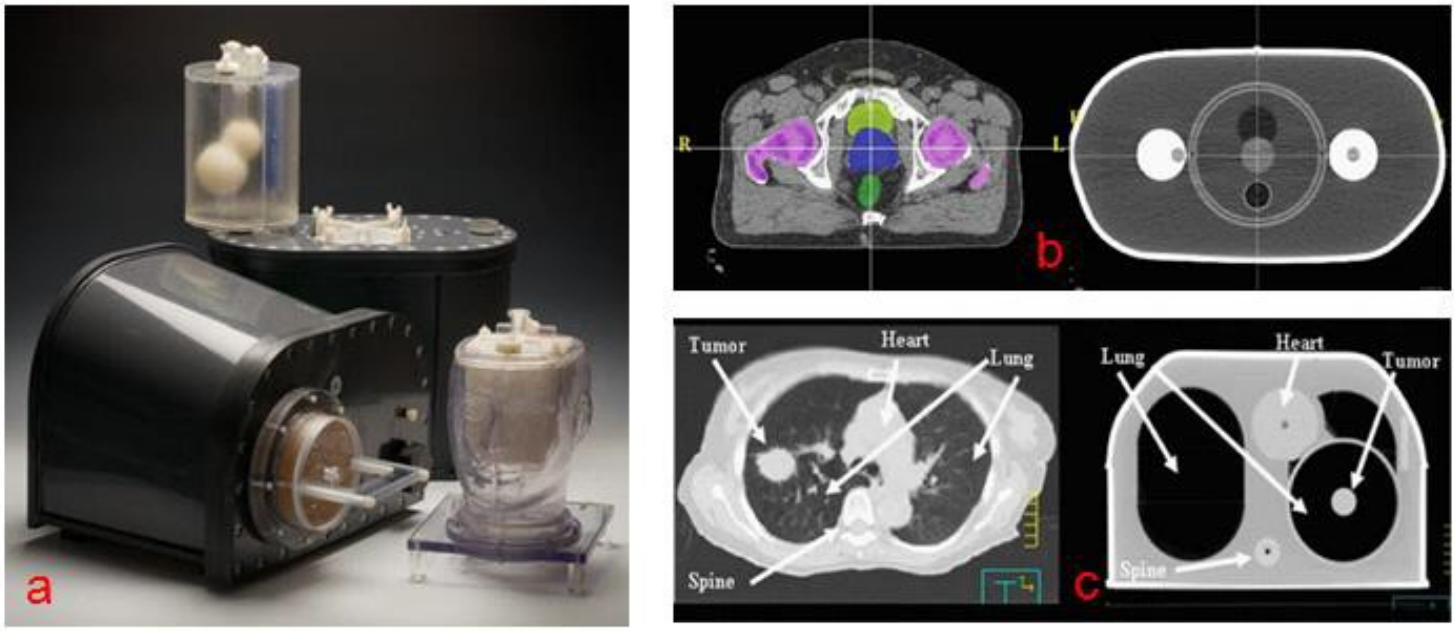

Figure 3, Currently available phantoms for head and neck, pelvis and lungs. (a) Photograph of external view, (b) CT images of a prostate patient (left) and pelvic phantom, (c) CT images of a lung cancer patient (left) and lung phantom. [13]

The in Figure 3 shown phantoms may just be a few examples of the lack in small level detail in currently commercially available phantoms, they also highlight the problem. These phantoms lack the desired millimetre scale level of detail, as the QA in proton therapy aims for accurate dose delivery within a few millimetres. [14] Therefore, a different production technique should be employed to create these phantoms at millimetre precision.

A promising candidate for this is Additive Manufacturing (AM), since this production technique is capable of both production at small levels of detail and with a great multitude of materials. How AM works and the possibilities to apply it as the new production method for phantoms will be discussed here.

Additive Manufacturing

Additive manufacturing, more commonly known as 3D printing, is a relatively new way of creating objects with high precision and a great level of detail. It differs from conventional

production techniques in the fact that, as the name states, it is additive and creates structures by adding material layer-by-layer, whereas conventional manufacturing (CM) processes are often of a subtractive nature, removing unwanted material by for instance drilling. This means that one of the mayor upsides to using AM over CM for the improvement of quality assurance in proton therapy, is the greater is design complexity that can be achieved with AM, since intricate designs are near impossible to create with CM. Therefore, this literature review aims to find the printing technique that is most applicable in quality assurance for proton therapy.

For the creation of the object, the first step in an either 4 or 5 step process that has to be taken, is to create a computerised 3D model, with the use of a Computer-Aided Design software package (CAD package), such as for instance SolidWorks® or Rhino®. The 3D model that has been created is then saved as a tessellated object: a triangulated representation of the model. This is saved as an .STL file, a Standard Tessellation Language file, in order for the AM system, which has to print the object, to understand it. Subsequently, the data file is sliced into layers, which the AM device will print. If so desired and depending on the complexity of the object, it may be that a fifth step is required to finish the object, which can be for instance polishing, sanding or painting. After this last step, the product is ready for use. [15] The whole manufacturing process is schematically shown in Figure 4.

When the object does not require any post-processing, it is considered a direct AM process. On the other hand, if it does require post-processing, the method is referred to as an indirect AM process [16].

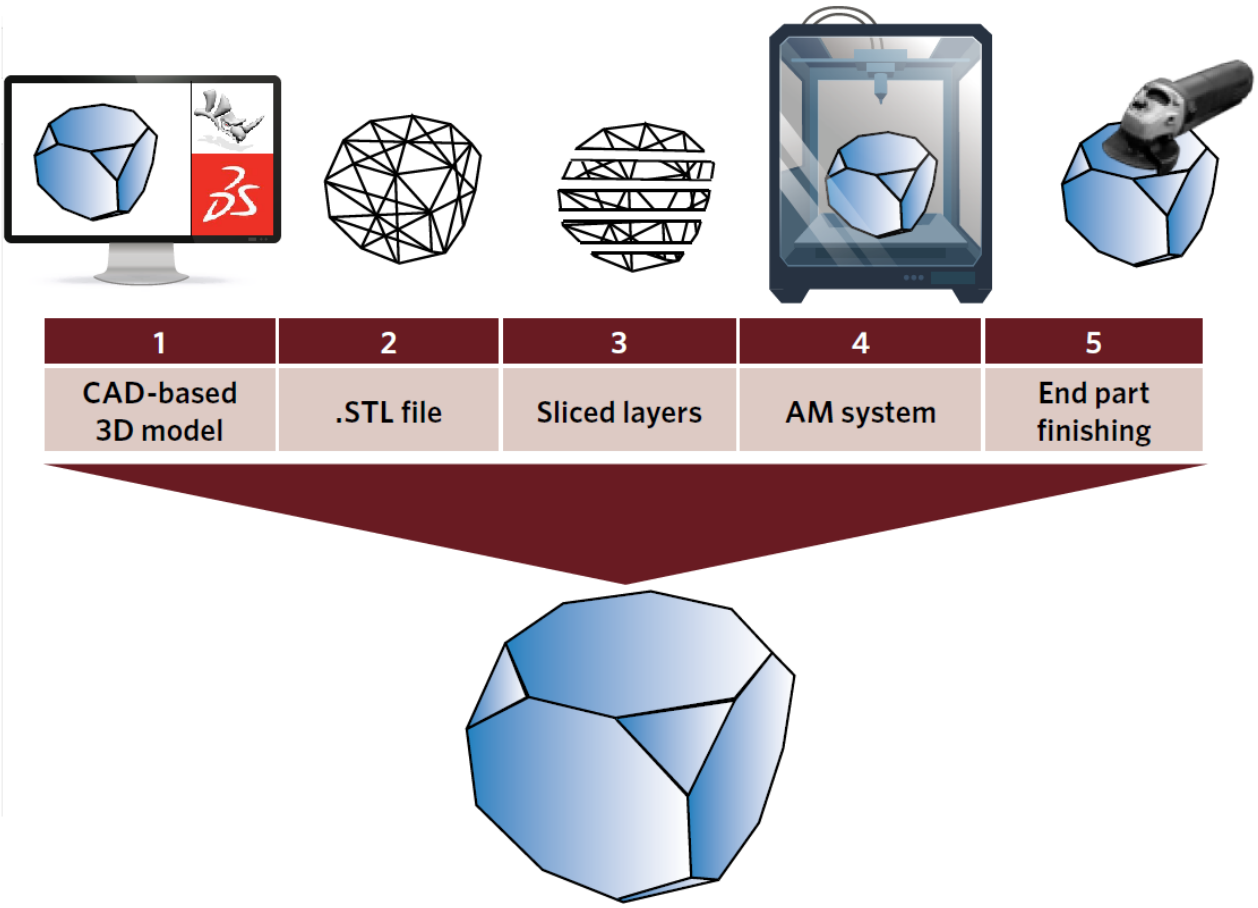

Figure 4, AM pipeline, from computer model to finished object. Adapted from [15].

AM processes

Within AM, there is a multitude of different techniques using which the system can build up the object layer-by-layer, creating two-dimensional layers on top of each other, resulting in a three-dimensional object. The most commonly used table-top consumer AM process is Fused Deposition Modelling (FDM), which works with, among others, polymers or thermoplastics. [16] A schematic of this method is shown in Figure 6 and will be discussed in greater detail further on.

As shown in Figure 5, even when only considering polymeric printing materials, there is a great multitude of different printing processes. Next to the aforementioned FDM, there are other printing techniques, which influence the materials available for printing, the accuracy and the print speed. [15] [16] [17] [18] These techniques are Powder Bed Fusion (PBF), Binder Jetting (BJ), Vat Photopolymerisation (VPP) and Sheet Lamination (SL). Some of the aforementioned printing techniques can also use metallic printing materials, but there are also techniques that are specific to metals such as Direct Energy Deposition (DED) and Ultrasonic Additive Manufacturing (UAM). A selection of techniques available in AM with metals are shown in Figure 11. [15] [16] [18]

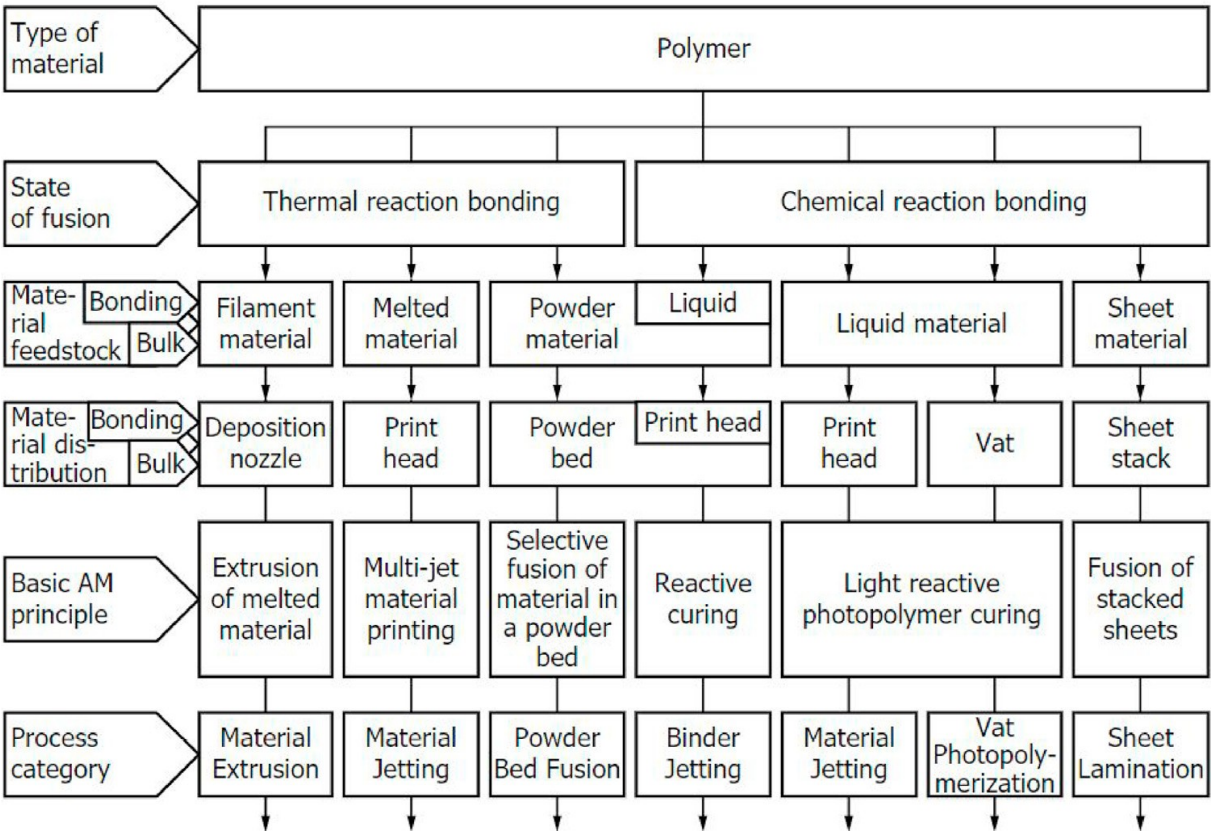

Figure 5, Schematic overview of single-step AM processing principles for polymeric materials. [16]

Within the printing processes listed in Figure 5, a distinction can be made on the primary heat source used to melt or weld the material, resulting in a different printing technique. For instance, in FDM, a heated nozzle is used to melt the plastics. Next to these heated nozzles, it is possible to melt the printing material using lasers, electron beams, plasma arcs and gas metal arcs. [16] For convenience, if there are multiple heat sources possible for a printing method, throughout this report the heat source will be added to the abbreviation of the printing techniques as a suffix. This will respectively be -L, -EB, -PA and -GMA. As an

example, this means that Direct Energy Deposition with a Laser becomes DED-L and Powder Bed Fusion using an Electron Beam becomes PBF-EB.

Fused Deposition Modelling

Within FDM, there are two main ways in which the printing material is deposited: Material Jetting (MJ) and Material Extrusion (ME). Both methods share a few common factors, such as the materials they can print with: either polymers (thermoplastics) or waxes. These materials are fed into a heater as a filament, then go through to the print head, or extruder, which than deposits the material on the print plateau. Specific to MJ, the extruder selectively deposits the printing material as droplets onto a build platform. This method can be expanded into Multi-jet modelling (MJM), where an additional extruder is incorporated in the 3D printer. An added benefit of MJM is that this gives the user the liberty to print with multiple materials simultaneously. When applying ME, the thermoplastic filament is fed through the heated nozzle which melts the material and deposits it onto a build platform. [15] Contrary to MJ, this is not done in droplets but as a continuous stream of material. A schematic of FDM is shown in Figure 6. This figure also shows support material, this is required in certain objects where the overhang is too large to support itself when the polymers are still warm.

In both MJ and ME, the available printing resolution in both the horizontal and the vertical direction depend on a few factors: the temperature at which the printer operates in combination with the material used, the quality of the filament and the way in which the filament is fed into the nozzle. Furthermore, in the case of MJ, the size of the deposited droplets. The operating temperature of the FDM printer has to be high enough for the filament to melt, so that it can be extruded by the nozzle, however the heater cannot become too hot, as that can cause undesired reactions in the material, such as, in the worst case, (partial) evaporation of the printing material. Also, if the material becomes too hot, it will flow out before setting, thus there will be a degeneration of the horizontal resolution, but if it becomes too cold, the vertical resolution may suffer due to the droplets not flowing out enough or the layers might not attach properly. Furthermore, the filament must be of high quality, since if it is thicker in some places, it will result in temperature differences and thus different levels of melting. Also, the feeding must go smoothly, the tension on and compression of the filament must not cause the filament to tear or tangle up, both before and after melting. [16] Lastly, the droplet size in MJ influences the resolution as well, since, also depending on the temperature, a larger droplet will spread out more, lowering the achievable resolution in the horizontal plane, yet a smaller droplet is more susceptible to disturbances from, for example, air flow, and may cool down too fast for proper deposition and attachment. Furthermore, the smallest achievable resolution of the printer is fixed by the smallest producible droplet size.

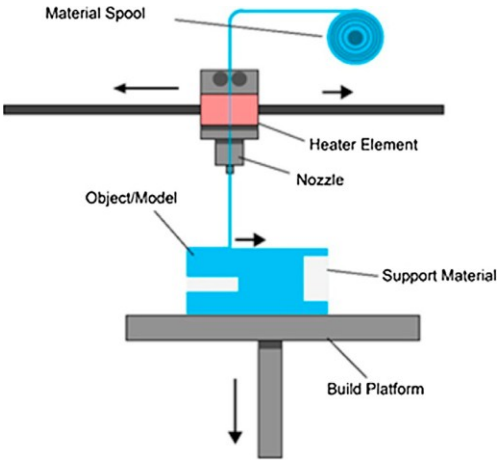

Figure 6, Schematic of a FDM AM system. [16]

Powder Bed Fusion

In Powder Bed Fusion, small particles of the printing material are melted together using a heat source such as a laser or an electron beam (PBF-L and PBF-EB respectively). After a layer is created, a new layer of powder is added on top of the object and the process is repeated. An advantage of this method is that any powder that has not been melted into the object, remains on the print platform, thus becoming support material for subsequent layers and therefore reducing the need for support systems. [15] [16] [18]

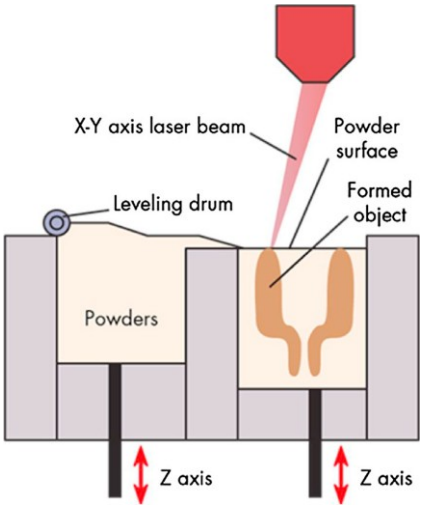

Figure 7, Cross section of a Powder Bed Fusion AM system. [16]

Both Figure 7 and Figure 11(d) show a schematic of this method. It can be clearly seen that there is a reservoir of powder, which can be spread over the top of the object using the levelling drum. It furthermore shows that there is no need for extra material to support the overhanging parts of the object, as the complete object rests upon unfused powder material. Another advantage of PBF is that by carefully controlling the amount of powder which is added on top for each consecutive layer, a high resolution in the vertical direction can be achieved. The resolution in the horizontal plane is defined by the width of the focus of either the laser or the electron beam.

The decision whether to use PBF-EB instead of PBF-L comes with a few difficulties that have to be overcome, the main two difficulties being that the procedure has to take place in vacuum and that the choice for PBF-EB limits the material choices to electrically conductive powders. [18] Furthermore, one has to realise that the powder will be charged electro-statically and may start to repel each other. This is done by first lightly sintering the powder

before scanning the surface again with the electron beam to fuse the powder together in the desired locations. This sintering has another advantage, namely that it causes the overall temperature of PBF-EB to be higher compared to PBF-L, thus it can scan the printing surface relatively faster.

Binder Jetting

Another printer that uses a powder bed, is a Binder Jet. Instead of a heat source to fuse the powder, a liquid binding agent such as glue is used. [15] [18] Just like in PBF, it is possible to use both polymeric and metallic materials, which is also spread on top of the previous layer with the levelling drum. In addition to the binding agent, it is possible to also include ink to colour the object during the printing phase. A schematic overview of this printing technique is shown in Figure 11(f).

Since PBF and BJ both use a similar material deposition in the form of powders, for BJ it also holds that there is no need for support material. The quality of the powdered material also has a great influence on the quality of the printed object. If the powder is of higher quality, both the powder packing characteristics and spreading uniformity, which will result in less deviation of the binding material from the desired location and thus higher accuracy in the end product. [17]

Vat Photopolymerisation

With Vat Photopolymerisation, the powder bed is replaced by a liquid. This printing technique uses a liquid resin like epoxy or acrylic, or liquid plastic that polymerises under exposure to UV light, called curing. This mostly is done with a UV laser. [15] [16] [19] As shown in Figure 8, there are two ways in which the resin can be exposed to the laser. Either by stereolithography (SLA), in which the resin is scanned with a laser (Figure 8(a) and Figure 8(b)), or by Digital Light Processing (DLP), in which a digital mask is projected in order to create the pattern. [16] Both SLA and DLP require post-curing of the object by a UV lamp to increase the structural integrity of the object.

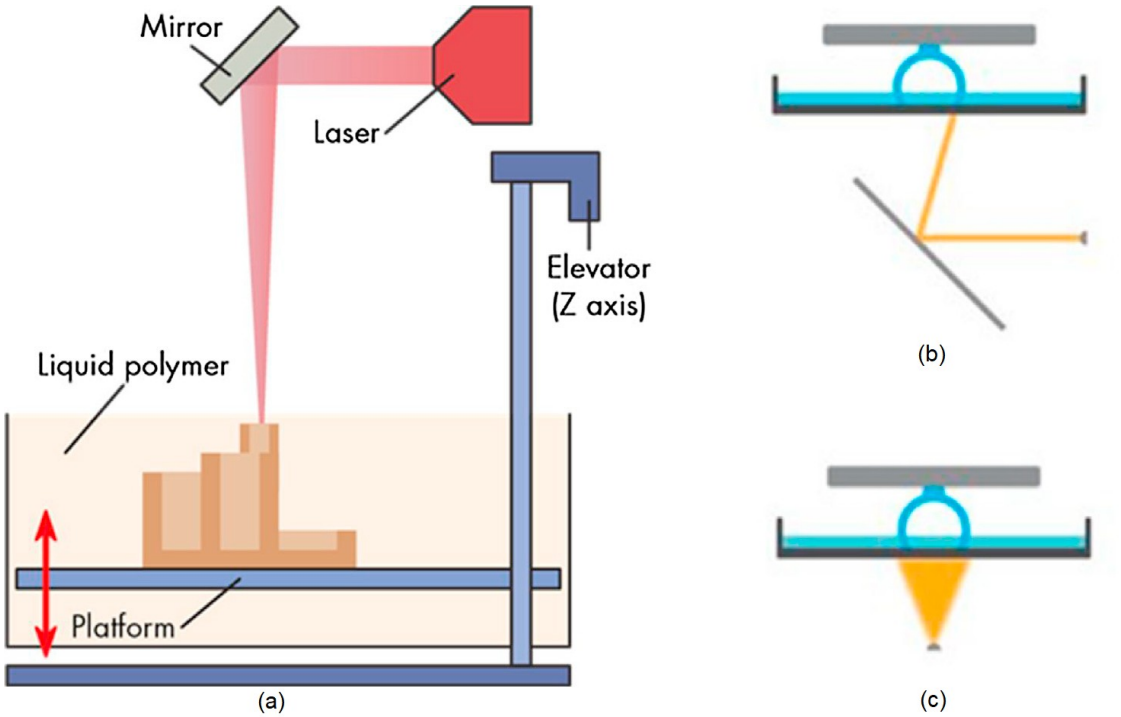

Figure 8, Schematic of a VPP AM system, (a) SLA with laser exposure from the top, (b) SLA with laser exposure from the bottom, (c) DLP. Adapted from [16].

Within SLA, you can then make a further distinction on the basis of the beam direction. It can be either be directed from the top (SLA-top, Figure 8(a)), thus the building platform moves from the top of the resin reservoir to the bottom, or it can be used to illuminate from the bottom (SLA-bottom, Figure 8(b)), therefore the building platform moves upwards, pulling the object out of the resin. Since the UV-light will initiate polymerisation along its whole path through the resin, it is crucial to control the fluid level carefully. This in itself is also an advantage of this printing method: if you can carefully control the depth at which the print plateau is submerged, you can achieve a thin layer thickness and thus a high resolution in the vertical direction. Typical layer thicknesses for SLA are in the range of 100µm, yet there are printers commercially available that are capable of a layer thicknesses of 25µm. [16] [20] The resolution in the horizontal plane is defined by the width of the laser beam. This is in the order of 85µm, but with this laser spot size it is also possible to achieve a resolution in the horizontal plane of 25µm. [20]

On the other hand, both SLA-top and SLA-bottom come with their own downsides: when illuminating from the top, you always need the resin bath to be filled to at least the height of the object you want to print, since otherwise your resin bath will run dry. In SLA with light exposure from the bottom, this is not necessary, but since the object is ‘pulled out’ of the resin, it needs to be attached to the plateau. Furthermore, creating objects which have structures that have overhanging parts is impossible to do without having to post-process the object, as it requires support structures to be printed along with the object, an example of these support structures is shown in Figure 9. The advantage for both forms of SLA is that, since there is no nozzle involved in this way of printing, clogging of the material is not a problem.

Figure 9, Object printed with SLA-bottom, with support structures. [20]

A technique very similar to SLA is DLP. The main difference between both methods is that instead of scanning the laser across the surface to solidify the desired parts of the resin, a digital mask from UV light is projected on the resin to create the desired pattern. When comparing this to SLA, the printing speeds of DLP can be far higher, as each complete layer is illuminated at once rather than scanning the entire layer. This comes at a cost in resolution. Since DLP projects a digital image, the pixel size of the projected image

determines the resolution, which differ from print to print depending on the amount of scaling done in the projection. Although this higher printing speed is advantageous when you need to print multiple large and compact objects with little detail, when the object has small details, you will require a projection lens that focuses the light on certain areas of the printing platform to be able to generate the required resolution. Generally speaking, SLA has a higher resolution and better surface finish than DLP, but longer printing times.

Sheet Lamination

Sheet Lamination is when thin sheets of material, such as plastics or metals, are bound together using a variety of ways, such as by ultrasonic welding or with glues. The new layer of material is placed on top of the previous layers, after which it is cut using, for instance, a laser or a knife to remove all unnecessary material. [15] [16] [18]

This printing method is also referred to as Laminated Object Manufacturing (LOM), which is shown in Figure 10. In this technique, it usually is the case that a sheet of material with a heat-activated adhesive is rolled out onto the printing platform via a heated roller. After it is applied, the layer is laser-cut into the desired shape and the remainder of the material applied in that layer is then disposed of to the waste roll. Furthermore, overhanging structures are not a problem in LOM, since the object made with LOM is self-supporting. However, it takes quite a long time to remove any excess material, especially when printing complex geometries. Furthermore, it has a rather poor surface finish, therefore requiring post-processing of the object. In addition, the resolution in the vertical direction is not completely controllable, as it depends upon the thickness of the sheet used and on how well the separate layers attach to each other. [16]

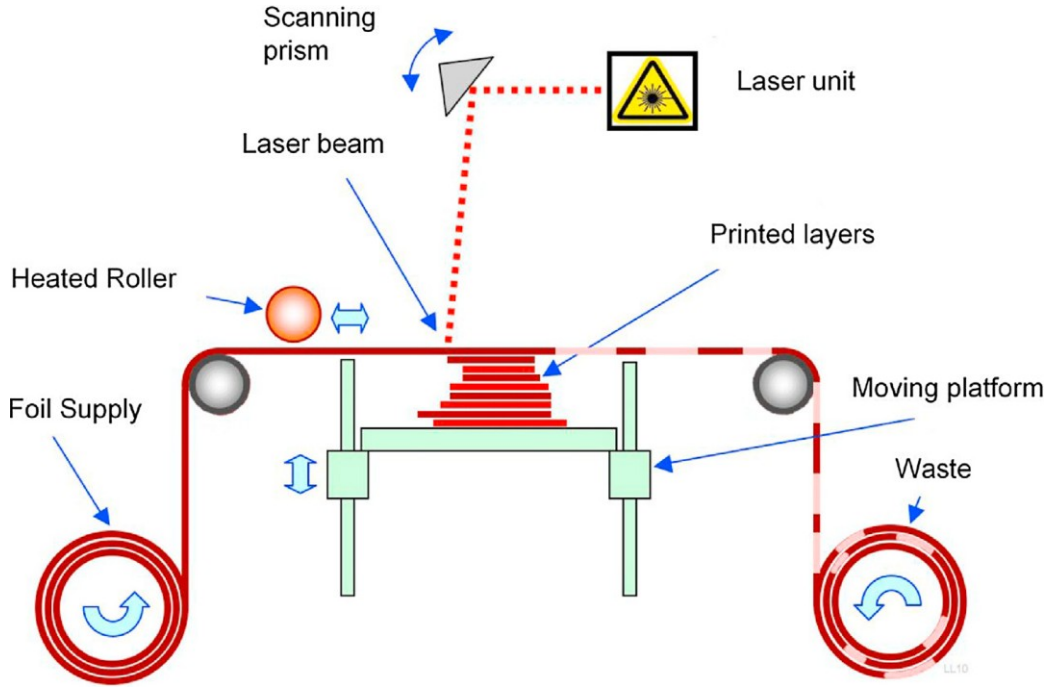

Figure 10, Schematic representation of LOM. [16]

When this printing method is applied to metallic sheets that are joined together using ultrasonic vibrations of the sheet under a constant normal force, it is called Ultrasonic Additive Manufacturing. The material is heated by these ultrasonic vibrations, thus softening them up, the normal force makes the layers adhere to each other. The vibrations are not powerful enough to melt the layers, thus they are joined together in solid-state. [18] This is shown in Figure 11(e). After welding together, the desired shape is cut out with for instance a laser.

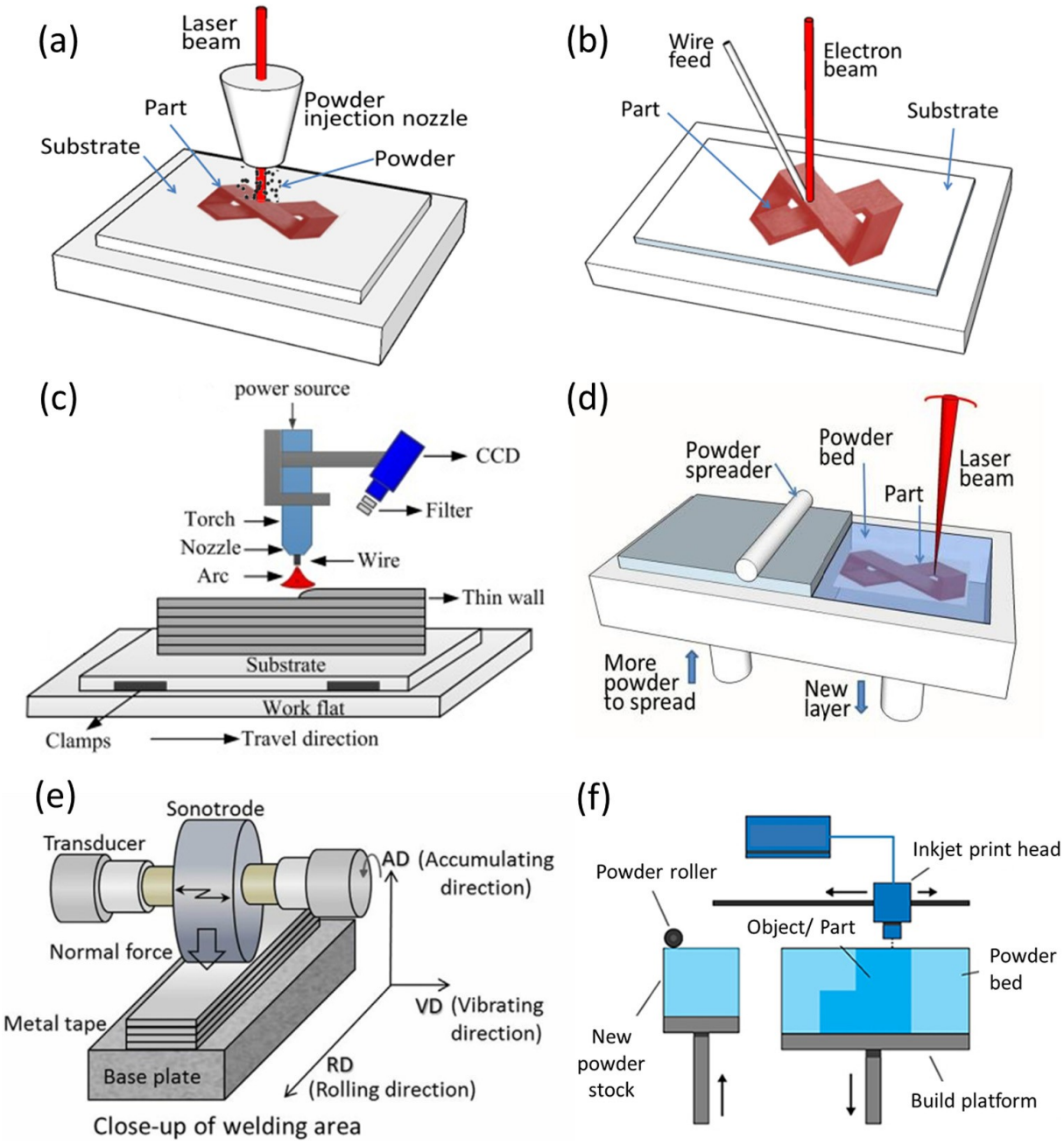

Figure 11, Schematic diagram of different printing techniques. (a) DED-L, (b) DED-EB, (c) DED-GMA, (d) PBF-L, (e) UAM, (f) binder jet. [18]

Direct Energy Deposition

When looking at metal printers, there is one last group of printers, which print by use of Direct Energy Deposition. In DED, a heat source is focused to fuse together material as it is being deposited, either as a powder or as a wire. To this group belong for instance DED-L, DED-EB and DED-GMA, show in Figure 11(a-c), respectively. In the first two techniques, a heat source creates a molten pool to deposit the material layer-by-layer. Furthermore, all three techniques use a different way in which the printing material is fed into the system, which is either as a powder, for DED-L, or as a filament wire, for DED-EB, DED-PA and DED-GMA. [15] [18]

In DED-L, the material is fed into the system through an injection nozzle as a powder, in the melt path of the laser and added into the molten pool. In order to shield the metal from immediate oxidation, a shielding gas such as argon is used. An added benefit of the

shielding gas is that it helps carrying the powder stream into the molten pool. [18] DED-EB works very similar to DED-L, as it feeds the material into a molten pool, but instead of a powder, it uses a wire filament as feed, and an electron beam as heat source. Furthermore, in order to be able to use an electron beam, DED-EB is performed under vacuum. This creates a high-purity environment in which the object is formed and can cool down in. In both DED-PA and DED-GMA, an electric arc is used to heat up a filament wire, therefore making this printing technique quite similar to fusion welding.

Print speed and accuracy

In the operation of AM systems, there is often a trade-off between printing accuracy and printing speed. For example, in PBF, the printing speed can be defined as the moving speed of the pool of material melted by the heat source, which in turn effects the spatiotemporal thermal characteristics. This will influence the printing quality, since the total amount of power transferred into the material depends on the total time the heat source is active in a certain area, which has an impact on the size of the pool of molten material, both in the horizontal plane as in the in the vertical direction, therefore in the resolution of the finished product. Furthermore, in SLA, the printing speed can be defined by the speed at which the laser is scanned over the surface. Similar to PBF, this has an effect on the curing of the resin, therefore on the achievable precision of printing. [17] For FDM systems, the kinematics of the extruder and the material used are the two main components controlling the print speed. Material with a lower melting temperature can be fed through the heater more quickly, improving the print speed. However, a higher print speed will result in a lowered deposition precision, since the faster the printing material is deposited, the more it will deform upon contact with the previous layer. [16] [17]

When looking at BJ, there are multiple parameters that can influence the print speed and precision, as well as the structural integrity of the finished object. Amongst others, these are the physical properties of the binding agent, the printing material used, the speed at which the print head moves, the volume of binding agent per droplets and the ratio between binging agent and powder. [17] The combination of these parameters will result in three phenomena that impact the droplet deposition: spreading, bouncing and splashing of the droplet. If the droplet bounces, the binding might occur in the wrong location. When the droplet spreads, the horizontal resolution deteriorates and with splashing, part of the droplet could end up in a location other than which is desired. The last two phenomena also cause a lower penetration of binding agent into the layer which is in the process of being printed, which in turn may result in a decreased adhesion between two subsequent layers, lowering the structural integrity of the object. To compensate for a decreased penetration depth of the binding agent, the drop volume can be increased. However, this comes at the cost of a greater amount of spreading and a reduced resolution.

A large factor in whether the droplet is spatially deposited as desired, is the velocity upon impact with a surface. This velocity has a significant impact on the flow dynamics of the droplet in porous media, such as the powdered material, due to inertia of the droplet. [2] At low velocity impacts, spreading is the dominant phenomenon, whereas at higher velocities, bouncing and splashing become dominant. Furthermore, the interplay between binding agent and powder material will also influence the level of spreading, splashing and bouncing, due to the chemical compatibility of the two materials.

Overview and outlook

An overview of the previously mentioned AM processes is shown in Table 1. Along with the most typical materials used per printing technique, a short list of advantages and disadvantages is presented as well.

Table 1, AM processes, most typical printing materials, advantages and disadvantages [15] [16] [17] [18] [19]

AM process	Printing technique	Typical materials	Advantages	Disadvantages
FDM	Material Jetting	Polymers, waxes	Good accuracy and surface finish, capable of multiple materials (multi-jetting), wide range of polymers, easy removal of support material	Relatively slow build process, limited range of wax materials available
	Material Extrusion	Thermo-plastics	Strong parts, capable of printing complex geometries	Relatively long build times and requiring post-processing due to medium surface finish
PBF	Laser melting	Plastics, metal, glass, paper, ceramic, composites	No need for support material, high printing speeds, high heat and chemical resistance	May require post-processing due to rough surface finish, accuracy limited by laser spot size and powder particle size
	Electron beam melting	Conductive metals	No need for support material, high printing speeds, limited distortion of parts	May require post-processing due to rough surface finish, accuracy limited by laser spot size and powder particle size, only works in vacuum with conductive metals
BJ	Binder jetting	Plastics, metals, composites	Inexpensive printing technique, ability to add colour during printing, no need for support material	Limited printing accuracy, requires post-processing due to poor surface finish
VPP	Stereolithography	Liquid photo-polymers, resins, composites	Ability to print highly complex geometries, smooth finish, high printing resolution	Post-curing required, needs support structures for overhanging parts

Table 1, continued

AM process	Printing technique	Typical materials	Advantages	Disadvantages
VPP	Digital Light Processing	Liquid photo-polymers, resins	High printing speed, can print complex geometries	Limited accuracy compared to SLA, requires post-curing, needs a projection lens when printing small details
SL	Laminated Object Manufacturing	Plastics, metals, laminates, paper, ceramics, composites	Relatively inexpensive printing method, quick to print large parts, no need for supporting material	Lower resolution in the vertical direction due to possible poorer adhesion between layers, removing excess material is time-consuming, possibly a lot of waste, requires post-processing
	Ultrasonic Additive Manufacturing	Metals, alloys	Quick to print large parts, fast adhesion with newer ultrasonic systems	Lower resolution in the vertical direction due to possible poorer adhesion between layers, removing excess material is time-consuming, possibly large amounts of waste, requires post-processing
DED	Laser melting	Metals, alloys	Capable to print with multiple materials, can build large parts, can print precise	Relatively high priced system, due to the need for a shielding gas, needs support structures, requires post-processing due to rough surface finish
	Electron beam melting	Metals, alloys	Capable to print with multiple materials, can build large parts, can print precise, high purity environment	Relatively high priced system, due to the need for a vacuum, needs support structures, requires post-processing due to rough surface finish

The overview presented in Table 1 is further compressed in Table 2. In this table, the applicability of the AM processes in proton therapy is shown. If for a specific process there are multiple techniques possible, then the most applicable technique is shown. This means that for FDM MJ is listed, for PBF this is PBF-L. In VPP the most applicable technique is SLA. For SL this is LOM, whereas in DED there is little to no difference, yet the choice is made for DED-L, since a shielding gas is slightly less inconvenient than a vacuum. A table with all the in Table 1 individually discussed AM processes is presented in Appendix A – Applicability of AM processes, in Table 10.

The table ranks the printing techniques based on the printable materials, the printing speed, the quality of the object and on other factors. The quality of the printed object is determined by the resolution of the print and the surface finish, the other factors are price and the need for support material and other conditions that have to be met in order to be able to print, such as the vacuum that is required for DED-EB and the possibility of waste production. Each category is ranked in the light of the requirements for a phantom suitable for quantifying the degeneration of the Bragg peak and for QA in proton therapy. Each process is ranked as very poor (- -), poor(-), intermediate (+/-), good (+) or very good (+ +).

Table 2, Applicability of AM processes. In case of multiple techniques for one process, the most applicable of the techniques is listed

AM process	Materials	Print speed	Quality	Other
FDM	+	-	+	+/-
PBF	+ +	+	+ +	+
BJ	+	+	+/-	+/-
VPP	+	+ +	+ +	+
SL	+	- -	-	+/-
DED	-	+	+/-	- -

Therefore, based on the data shown in Table 2, PBF-L and SLA are both very suitable for usage in proton therapy. Depending on how quickly the phantom has to be ready and on the specific application, the user can make a choice for either of these two printers. The specific application, the part of the body the phantom should represent, impacts the requirements on the materials, since soft tissues can be represented with polymers, yet dense tissues such as bone require heavier materials such as metals. Furthermore, one should however take into account that in both techniques it is essential to have a way of verifying that the object is printed as desired, since in both techniques there is a possibility for residual powder or resin to get trapped in a cavity and thus change the characteristics of the phantom.

The objects fabricated this way can, as proposed before, be used to help improve the quality assurance in proton therapy. This is also shown by J. Madamesila et. al [21], who produced a series of phantoms with different levels of infill which are checked with a CT scan and tested for their proton stopping power. With this, they show the effect of the incorporated air cavities to create the desired infill level.

Materials and methods

As mentioned in the Introduction, the aim of this study, is to find out if it is feasible to 3D-print a phantom that can be used to quantify the degradation of the Bragg peak due to tissue heterogeneity in lung proton therapy. This is done both by determining the limitations of the available 3D printers and by simulations based on the 3D printable designs in Monte Carlo.

3D printers

For this research, a pair of 3D printers were available. The first is an Ultimaker3, which is an MJM FDM printer, as described in the section Fused Deposition Modelling and shown in Figure 6. The Ultimaker3 prints with any filament that is 2.85mm in diameter, therefore allowing for a large variety of materials, however there is only a limited amount of materials commercially available for the Ultimaker3. The smallest string it is capable of printing is 400µm in the horizontal directions and 20µm in the vertical direction. Furthermore, this printer is not designed for printing large solid objects, which usually are printed hollow at only 20% of the total volume consisting of printed material, which is enough for the object to be strong enough to support itself.

The second is a Formlabs Form2, which applies the SLA-bottom printing technique, as described in the section Vat Photopolymerisation and is shown in Figure 9. The Form2 printer uses resins to print, thus printing is done in a single material. The laser used to cure the resin has a wavelength of 405nm, with a spot size of 140µm. The thinnest layer this printer can achieve is 25µm. After the print is made, this first has to be cured before it is strong enough to be used.

CAD software package

As mentioned in the section Additive Manufacturing, in order to generate a tessellated structure file that can be printed, a Computer-Aided Design software package is required. For this research, the choice was made to use the 2017 version of SolidWorks, by the French company Dassault Systèmes. This software package is used to generate the porous structures that are used in the simulations, as described in the next section Monte Carlo simulations. An example of such a structure is shown in Figure 12.

These structures are 2.5 dimensional: they comprise of a solid block with dimensions of 100mm by 100mm by 250mm (width, height, depth). Into this block, a selection of hollow cylinders is inserted, with radii of 0.5mm, 1.0mm or 1.5mm, which span the entire width and are stacked the whole height of the block. The distance between the edges of two cylinders within one layer is equal to one time the radius of the cylinder. The middle points of two subsequent layers are twice the radius of the cylinders apart. This is done either with just two vertical layers of cylinders, or as a multilayer porous structure as shown in Figure 12. These will be referred to as the bilayer and porous structure, respectively. In both structures, the

even numbered layers have the midpoints of their cylinders centred between the midpoints of the two cylinders directly in front for it.

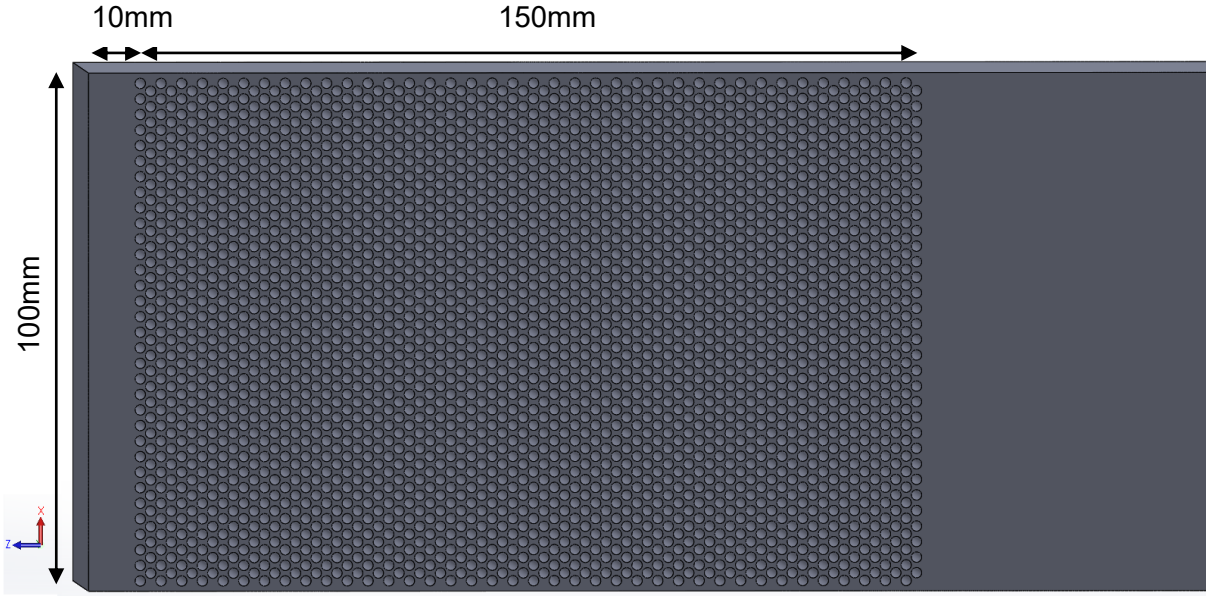

Figure 12, Side view of the porous structure in SolidWorks.

For both different structures, the first layer of cylinders has its centre located 10mm from the edge of the block. With the bilayer structure, the centre of the second and last layer is located twice the radius of the cylinders deeper into the block, thus at 11mm, 12mm, 13mm, 14mm and 15mm.

With the case of the porous structures the second layer follows the same layout as that of the bilayer structure. The subsequent layers form a regularised grid, which can be clearly seen in Figure 12, with the last layer is centred at a depth of about 160mm into the block. Therefore, the porous structures comprise of 150, 76 and 50 layers respectively. The choice for a depth of 160mm was made based on the fact that this coincides with the approximate location of the tail end of the Bragg peak for protons with an energy of 160MeV, after having passed through a single bilayer of hollow cylinders.

Monte Carlo simulations

The simulations are performed in Monte Carlo (MC), with the program TOPAS MC [22] that is an adaptation on the Geant4 simulation toolkit. [23] [24] The version utilised for this research was TOPAS 3.2.0/Geant4 10.05.p01.

The Geant4 material database from which this simulation toolkit gets the data on the chemical composition of the materials used, is the NIST database, as described by J. Meija et. al in [25]. From this the chemical composition and mean excitation energies of both in this research used Polyvinyl Alcohol (PVA) and air are retrieved. PVA ($(C_2H_4O)_n$, weight fractions H=0.091517, C=0.545298 and O=0.363185), has a mean excitation energy of 69.7eV and density of 1.3g cm^{-3}. The air comprises of a mixture of oxygen, nitrogen, carbon dioxide and argon, with weight fractions C=0.000124, N=0.755268, O=0.231781 and Ar=0. 012827. This mixture of gasses has a mean excitation energy of 85.7eV and density of 1.20479mg cm^{-3}.

The phantoms used in the simulations are both directly implemented as tessellated structures and as a direct build in TOPAS MC. An example of the latter is shown in Figure

13, which shows a side view of the PVA block, the edges of the block are indicated by the light blue lines. The red and white circles indicate the locations of the air filled cylinders. The proton beam is incident from the left hand side of the figure.

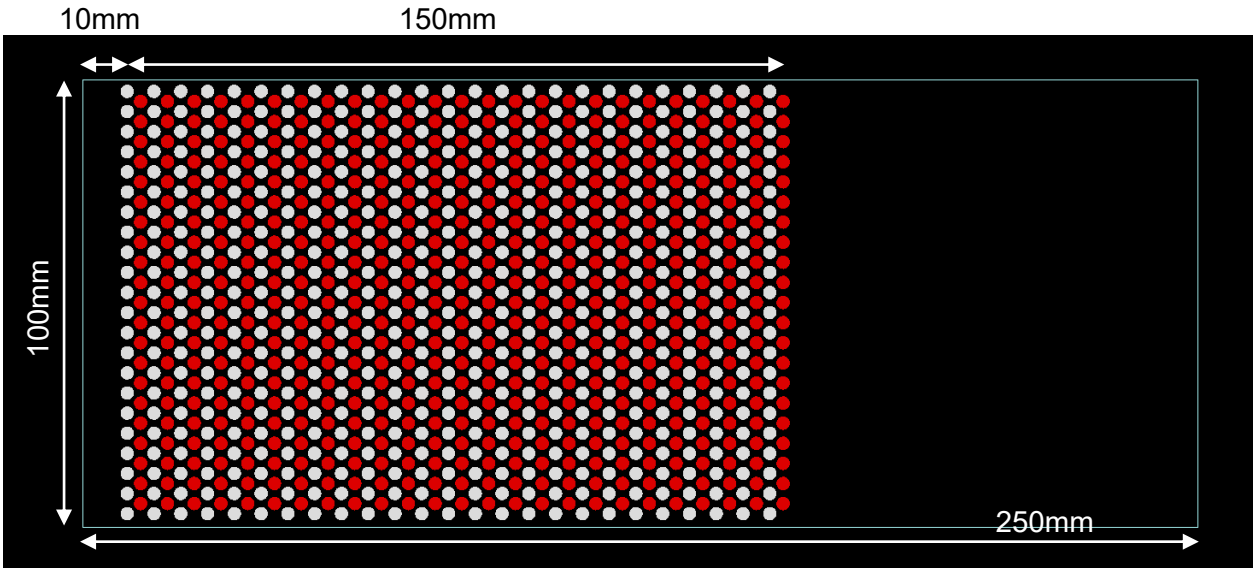

Figure 13, Side view of a porous structure in TOPAS MC. The red and white circles are the sides of the hollow cylinders, both with the same radius. The difference in colour is to make a clearer distinction between odd (white) and even (red) layers.

This proton source is a single pencil beam (SPB) and is modelled as a round source with a Gaussian distribution around its centre and uses $1.5 \cdot 10^6$ protons per simulation, at three different energies: 80MeV, 120MeV and 160MeV. The proton beam location is such that its origin is directly in the centre of the short side of the PVA block. An example a simulation with 150 particle tracks is shown in Figure 14. The resulting dose of these protons to the simulated phantoms is scored in a voxel grid of $2 \cdot 10^7$ voxels, each $0.5 \times 0.5 \times 0.5 mm^3$, which completely envelopes the PVA block, thus the light blue lines also indicates the scoring volume. The respective controls for the proton beam and scorer can be found in Appendix B – Example of TOPAS MC simulation, under the headers Beam 1 and Scorer. As can be seen in this appendix, both the Dose to Medium and to Water are determined for each simulation.

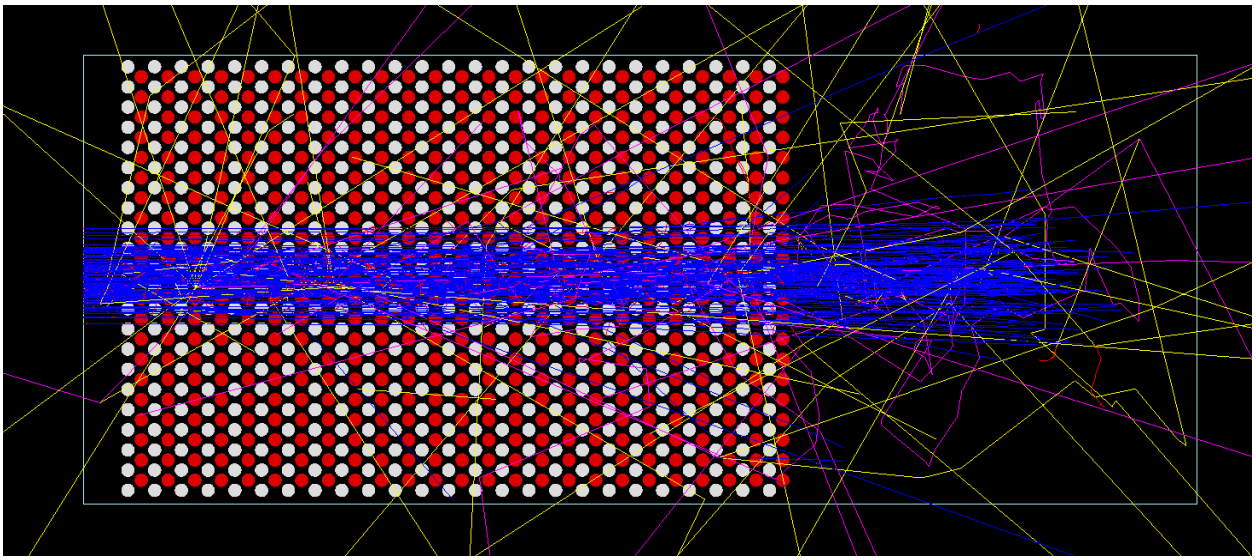

Figure 14, Same side view as in Figure 13, with 150 particles tracks of 160MeV protons visualised. The shown particles are protons (blue), electrons (red), gammas (yellow) and neutrons (magenta).

The resulting dose profiles are compared to that of a solid block of PVA, which is also irradiated with $1.5 \cdot 10^6$ protons and has an identical scoring voxel grid.

Lastly, a set of simulations is performed in which the porous structure is replaced by a section of PVA that matches the width and height of the block and has a density that has been adjusted to match the average density of the porous structure. The chemical composition of the PVA remains the same (weight fractions H=0.091517, C=0.545298 and O=0.363185) and mean excitation energy 69.7eV. The averaged density then is 0.63g cm^{-3}, which is equivalent to approximately 48% of the regular density. Next to this, some more extreme cases are tested, with the adjusted density ranging from 10–250% of the regular density.

The degeneration of the Bragg peak will be classified based on the following parameters:

- New Bragg peak location, thus the shift in Bragg peak location,
- Change in dose in the Bragg peak,
- 80% dose point after the Bragg peak,
- 50% dose point after the Bragg peak,
- 1% dose point after the Bragg peak,
- Full width at 80% of the maximum (FW80M),
- FW80M widening,
- Full width at half maximum (FWHM),
- FWHM widening,
- FWHM/R ratio,
- Length of the tail of the Bragg peak,
- Tail lengthening.

The tail length of the Bragg peak is defined as the distance of the Bragg peak location to the 1% dose point, and the ratio between the FWHM and the range is determined by the width of the Bragg peak and its own range. The widening of both FW80M and FWHM and the lengthening of the tail are compared to the relative quantities for the Bragg peak in solid PVA.

If the dose points are not located exactly in a voxel, a linear interpolation is performed to locate the dose point. This via interpolation determined location is then also used to determine the FW80M and FWHM and tail length. Furthermore, the isodose curves are compared visually.

Results

The result of the quality assessment of the 3D printing and the simulations in TOPAS MC are presented in this chapter. The results for the simulations are subdivided into bilayer, porous structures per proton beam energy and adjusted densities.

3D printing

The first objects produced with the Ultimaker3 3D-printer are shown in Figure 15 and Figure 16. The object in Figure 15 displayed has a height of 28.6mm and width of 30mm, with the beams having a thickness of 1.4mm. The angle between the diagonal beams is 90°. At this scale the printer is capable of creating the overhanging structures without the need for support structures and only requires minor post-processing.

After this first successful test print, two more prints were performed, to test its ability of the printer to manufacture larger objects with air cavities and the capability of printing angles greater than 90° between the diagonals without support structures. These objects are shown in Figure 16, with the left object having dimensions 30x30x13mm, the right object having the same dimensions as the object in Figure 15, but with angles of 100°, 110° and 120° between the diagonals (back to front respectively).

As can be clearly seen from the figure, both objects show significant malformations. It shows that the object on the left-hand side has undulations on the top layer, the right-hand side object shows the inability of the Ultimaker3 to print objects with a large overhang without support structures.

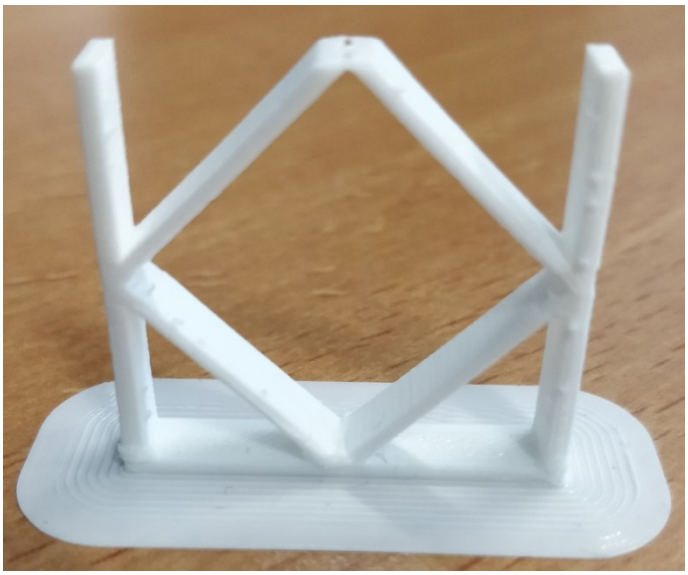

Figure 15, Photograph of a successful test print using the Ultimaker3 printer.

Figure 16, Photograph of two unsuccessful test prints using the Ultimaker3 printer.

The other available printer, the Form2, was not tested in a similar fashion as the Ultimaker3, but its technical specifications, as provided by the producer, [20] are used as a basis for the creation of the porous structures used in the simulations.

Monte Carlo simulations

All subsequent dose distributions will be compared to the in Figure 17 presented pristine Bragg peaks and in Figure 18 and Figure 19 presented isodose contours for a SPB.

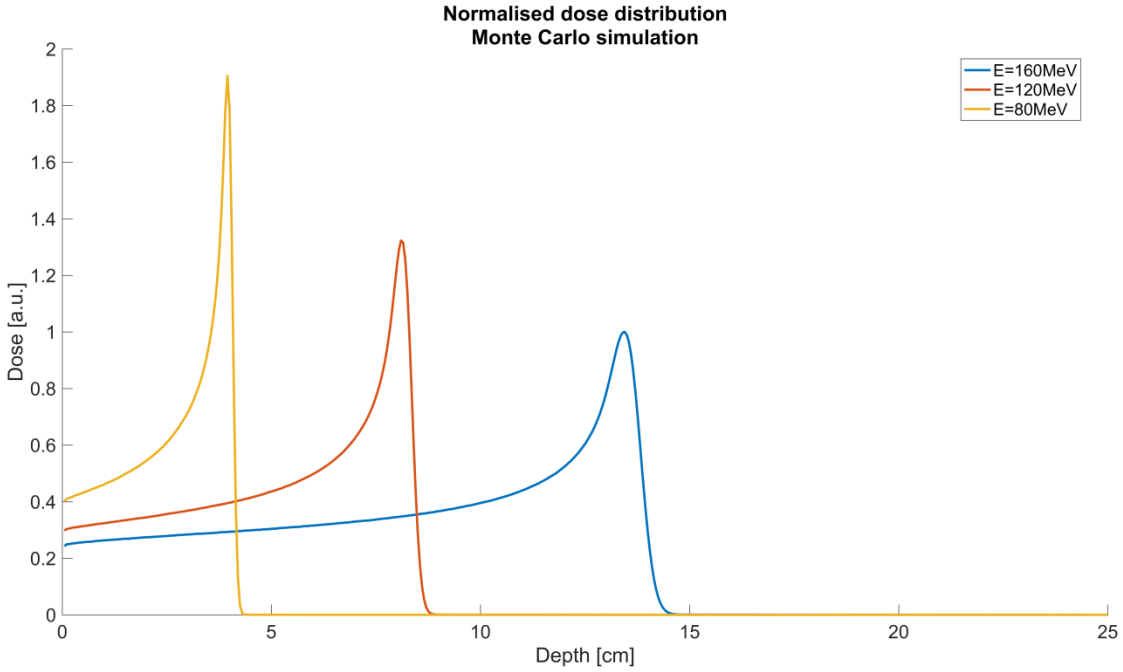

Figure 17, Pristine Bragg peaks in a solid block PVA, for proton beams with energies 80MeV, 120MeV and 160MeV. The dose is normalised to the dose by the 160MeV protons and determined as the dose in an entire slice.

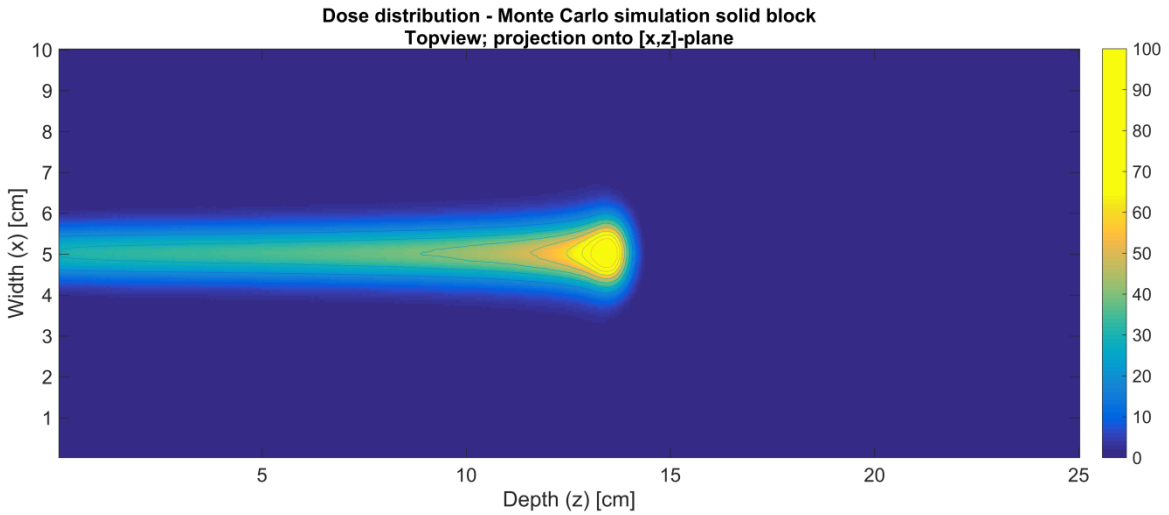

Figure 18, Normalised isodose distribution in a solid block PVA, for protons of 160MeV, dose projection onto the [x,z]-plane.

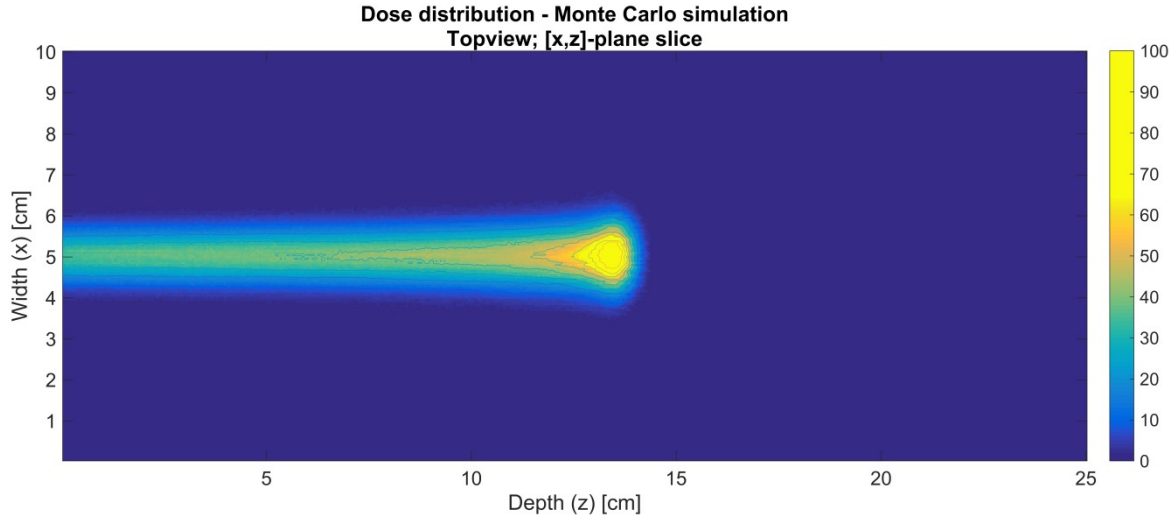

Figure 19, Normalised isodose distribution in a solid block PVA, for protons of 160MeV, dose sliced on the [x,z]-plane at y=5cm.

Since the solid block of PVA is symmetric, the dose distribution in the [x,z]- and [y,z]-planes are identical. Therefore, the presented isodose distributions of a dose projection (Figure 18) and dose slice (Figure 19) are both shown for only the [x,z]-plane.

Bilayer

From Figure 20, it can be seen that a bilayer in the PVA block causes the Bragg peak to shift slightly away from the entry point of the proton beam, this shift in the Bragg peak location is equal to the diameter of the inserted cylinders. The 80%, 50% and 1% dose points also translated deeper into the block, the magnitude of the shift is dependent on the size radius of the cylinders: a larger cylinder induces a larger shift in these dose point. This is also reflected in a larger FW80M and FWHM, and a longer tail length.

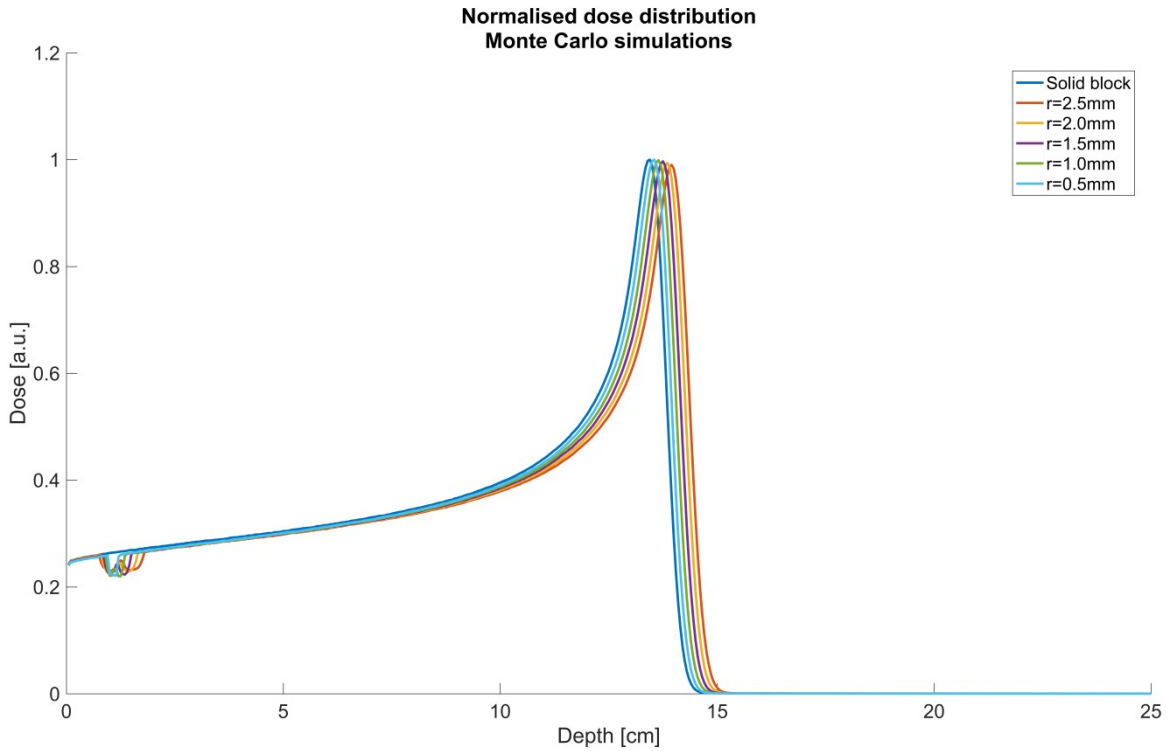

Figure 20, Normalised dose to the medium, in a solid block PVA and bilayer blocks with r=2.5mm, r=2.0mm, r=1.5mm, r=1.0mm and r=0.5mm, for proton beams with energy 160MeV. The dose is normalised to the dose by the protons in the solid block and determined as the dose in an entire slice.

Furthermore, it can be clearly seen that the cylindrical inserts cause a lowering in the dose distribution at their location. Also, the dose in the Bragg peak is slightly lower in the bilayer cases compared to the solid PVA block. This lowering of the peak height is also dependent on the radius of the cylinder: a larger cylinder means a lower peak. The numerical values for the bilayers are shown in Table 3.

Table 3, Numerical values for the bilayer blocks, for proton beams with energy 160MeV, as shown in Figure 20.

	Bragg peak location [mm]	Normalised dose Bragg peak [a.u.]	80% dose point [mm]	50% dose point [mm]	1% dose point [mm]	FW80M [mm]	FWHM [mm]	Tail length [mm]
Solid PVA	134.5	1	136.97	138.73	144.70	6.64	20.72	10.20
r=2.5mm	139.5	0.990	142.14	143.96	150.16	6.77	21.29	10.66
r=2.0mm	138.5	0.994	141.11	142.91	149.00	6.73	21.15	10.50
r=1.5mm	137.5	0.997	140.08	141.86	147.87	6.68	20.87	10.37
r=1.0mm	136.5	0.999	139.05	140.81	146.80	6.63	20.77	10.30
r=0.5mm	135.5	1	138.02	139.77	145.70	6.64	20.67	10.20

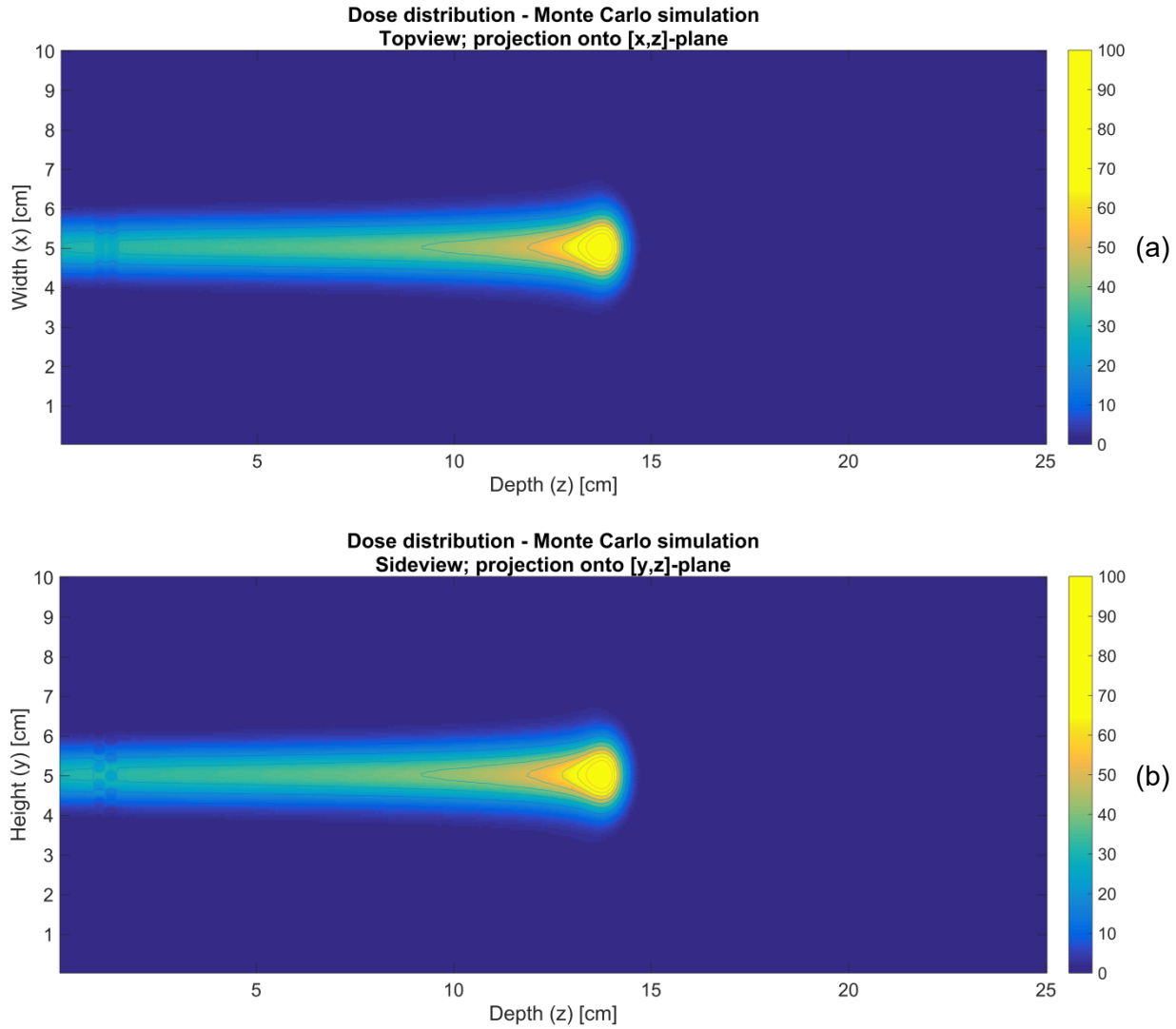

Figure 21, Normalised isodose distribution in bilayer block with cylinders r=1.5mm, for protons of 160MeV. (a) Dose projection onto the [x,z]-plane, (b) dose projection onto the [y,z]-plane.

In Figure 21 and Figure 22, the normalised dose distributions are shown for the bilayer case with cylinders of r=1.5mm. For both figures, the isodose distribution shown in (a) is that on the [x,z]-plane, with the [y,z]-plane distribution shown in (b). The other bilayer cases are not shown, since these follow a similar layout and only the size of the cylindrical holes are of a different size.

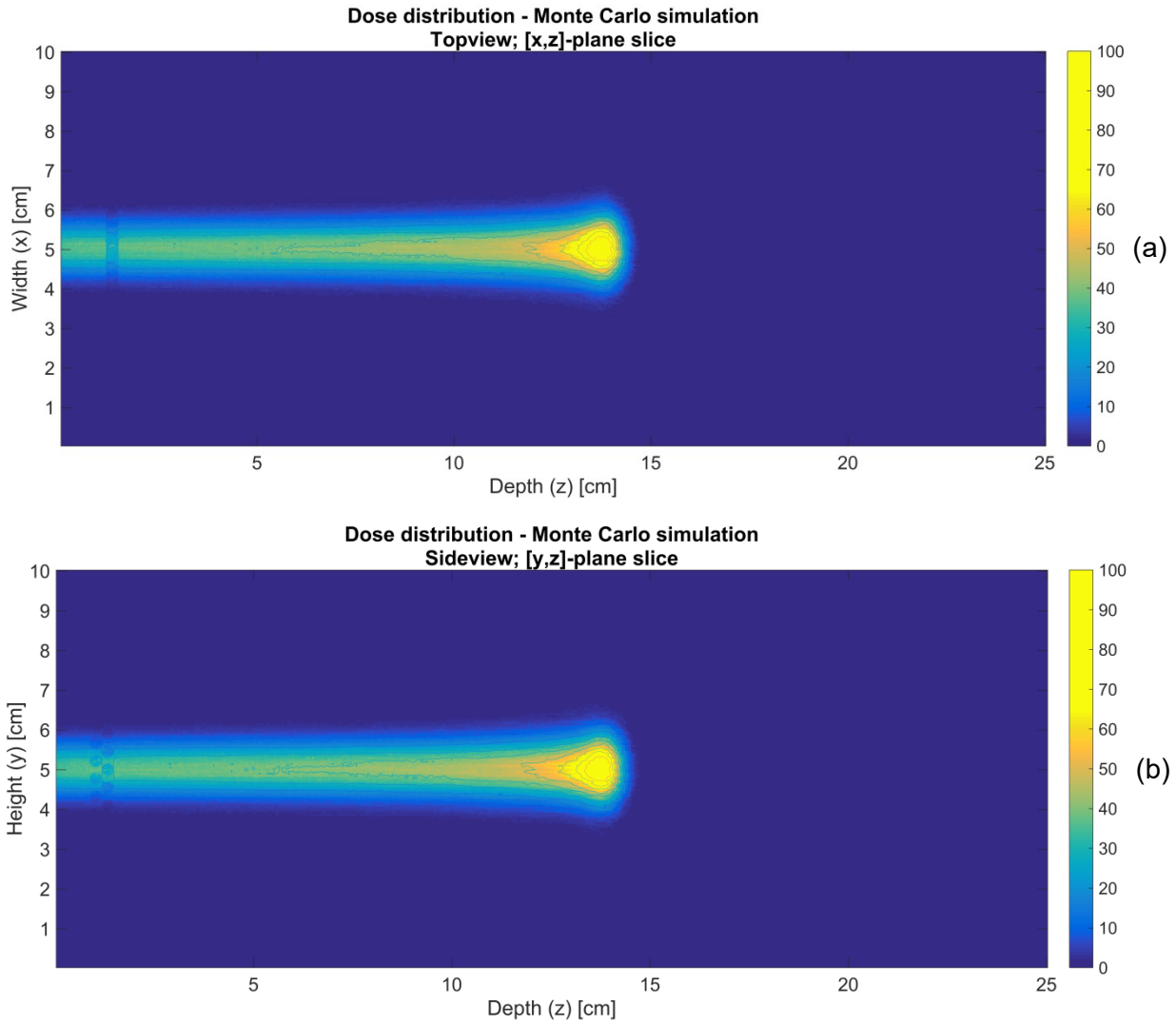

Figure 22, Normalised isodose distribution in bilayer block with cylinders r=1.5mm, for protons of 160MeV. (a) Dose sliced onto the [x,z]-plane at y=5cm, (b) dose sliced onto the [y,z]-plane at x=5cm.

Porous, E=160MeV

The normalised dose to medium for proton beams with 160MeV are shown in Figure 23 and Figure 24, for simulations on tessellated structures and direct builds in TOPAS MC respectively. The first thing that should be noted, is that for the simulations on tessellated structures, these have both very long runtimes during the simulation (simulation times of over two weeks) and significant losses due to simulation errors (up to 50% of the tracks resulting in an error for the smallest porosity), which caused TOPAS MC to remove the entire incident from the simulation. This results in a significantly lowered dose. This is further enhanced by the fact that, the simulation with the smallest porosity (r=0.5mm) was performed with only $1.2 \cdot 10^6$ protons, in order to keep the simulation times within more reasonable limits. Also, from Figure 24, it can be seen that the tail end of the Bragg peak reaches further than 25cm, therefore is no longer in the scoring volume, thus the 1% dose point and tail length for this Bragg peak cannot be determined.

From both figures, it can also clearly be seen that the introduction of porosity causes the Bragg peak to have a significant translation in the direction the proton beam travels. Also, just like in the case with the bilayers, the Bragg peaks become both lower and are broadened.

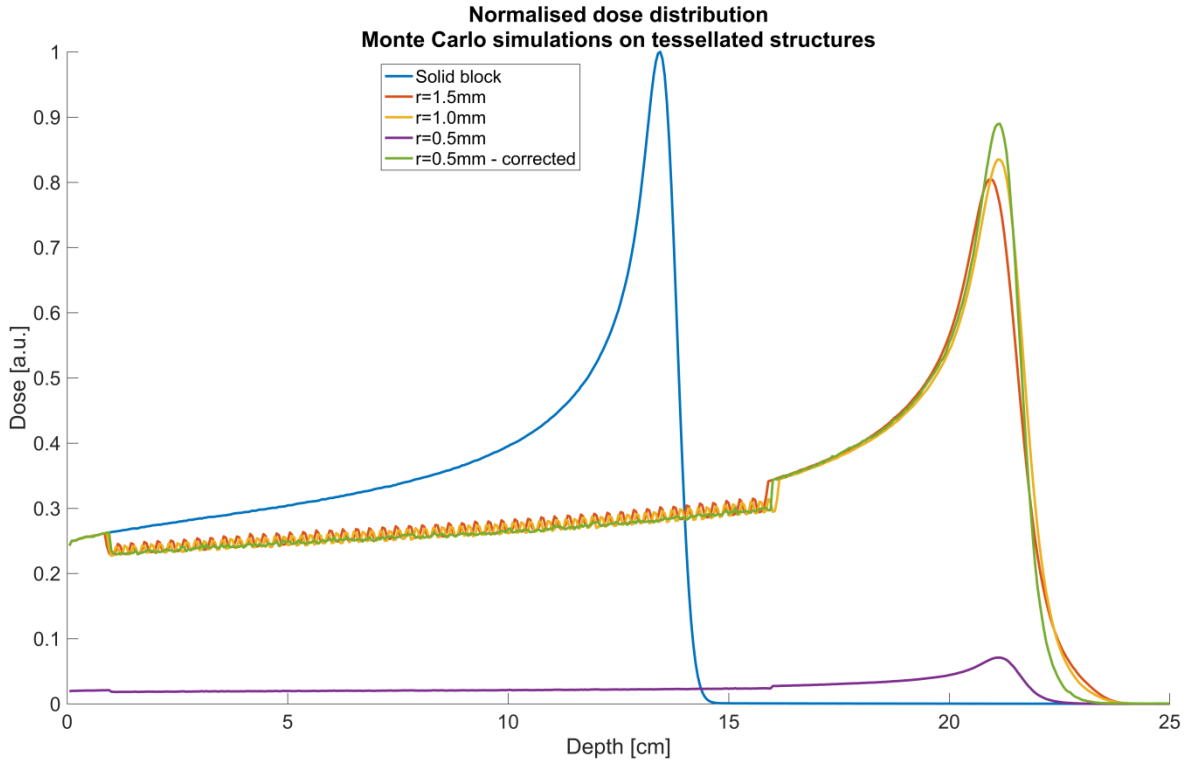

Figure 23, Normalised dose to the medium, in a solid block PVA and porous structures from tessellated structures, with r=1.5mm, r=1.0mm, r=0.5mm, for proton beams with energy 160MeV. The dose is normalised to the dose by the protons in the solid block and determined as the dose in an entire slice.

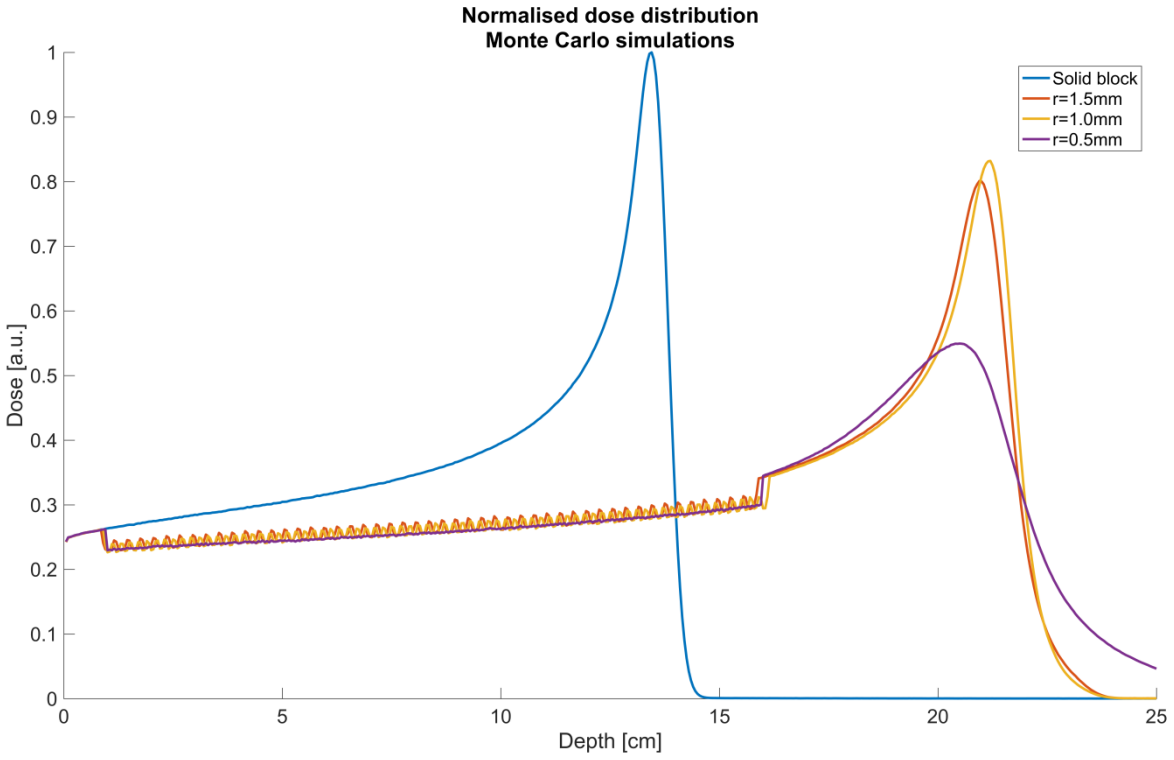

Figure 24, Normalised dose to the medium, in a solid block PVA and porous structures direct built in TOPAS MC, with r=1.5mm, r=1.0mm, r=0.5mm, for proton beams with energy 160MeV. The dose is normalised to the dose by the protons in the solid block and determined as the dose in an entire slice.

Furthermore, it can be observed that for both the simulations on tessellated structures as on direct builds in TOPAS MC, the dose distributions for r=1.5mm and r=1.0mm show identical trends, which can also be seen from the near identical numerical values for these dose deposition profiles in Table 4. For the r=0.5mm porosity, the dose depositions show a significant shift in the location of the Bragg peak, the 80% dose point is for both cases in the same location, yet the 50% dose point is closer to the entry point of the proton beam in the tessellated structure case. Furthermore, the width of the Bragg peak for simulation directly built in TOPAS MC is about 3.5 times larger than simulations performed on tessellated structure, both the FW80M and FWHM.

Table 4, Numerical values for the porous structues, for proton beams with energy 160MeV, as shown in Figure 23 and Figure 24.

	Bragg peak location [mm]	Normalised dose Bragg peak [a.u.]	80% dose point [mm]	50% dose point [mm]	1% dose point [mm]	FW80M [mm]	FWHM [mm]	Tail length [mm]
Solid PVA	134.5	1	136.97	138.73	144.70	6.64	20.72	10.20
r=1.5mm	209.5	0.801	214.09	217.44	236.52	10.57	37.07	27.02
r=1.5mm .stl	209.5	0.805	213.73	216.98	235.85	10.44	36.52	26.35
r=1.0mm	212	0.832	215.62	218.47	235.46	9.84	33.29	23.46
r=1.0mm .stl	211	0.835	215.25	218.07	234.82	9.78	32.96	23.82
r=0.5mm	205	0.549	214.09	221.18	-	29.17	97.7	-
r=0.5mm .stl	211.5	0.071	214.63	217	229.31	8.6	27.68	17.81

Table 5, Shift and widening of the Bragg peaks in porous structures compared to solid PVA, for proton beams with energy 160MeV.

	Bragg peak shift [mm]	Relative range	FW80M widening	FWHM widening	FWHM/R	Tail lengthening
r=1.5mm	75	1.558	1.592	1.789	0.177	2.649
r=1.5mm .stl	75	1.558	1.572	1.763	0.174	2.583
r=1.0mm	77.5	1.576	1.482	1.607	0.157	2.300
r=1.0mm .stl	76.5	1.569	1.473	1.591	0.156	2.335
r=0.5mm	70.5	1.524	4.393	4.715	0.477	-
r=0.5mm .stl	77	1.572	1.295	1.336	0.131	1.746

Figure 23 also shows a corrected normalised dose distribution for cylinders of r=0.5mm. This correction has been performed by extrapolating the successful proton events to correspond to $1.5 \cdot 10^6$ protons. For the corrected normalised dose, it holds that all values presented in Table 4 are identical to the non-corrected values, except for the normalised dose in the Bragg peak, this value becomes 0.89 a.u.. Furthermore, the FWHM/R ratio for the protons in solid PVA is 0.154.

As Table 5 shows, for all simulations the relative range is almost identical. However, when disregarding the simulation with tessellated structures with r=0.5mm, the FW80M, FWHM, Tail lengthening and FWHM/R ratio are larger for larger cylinders.

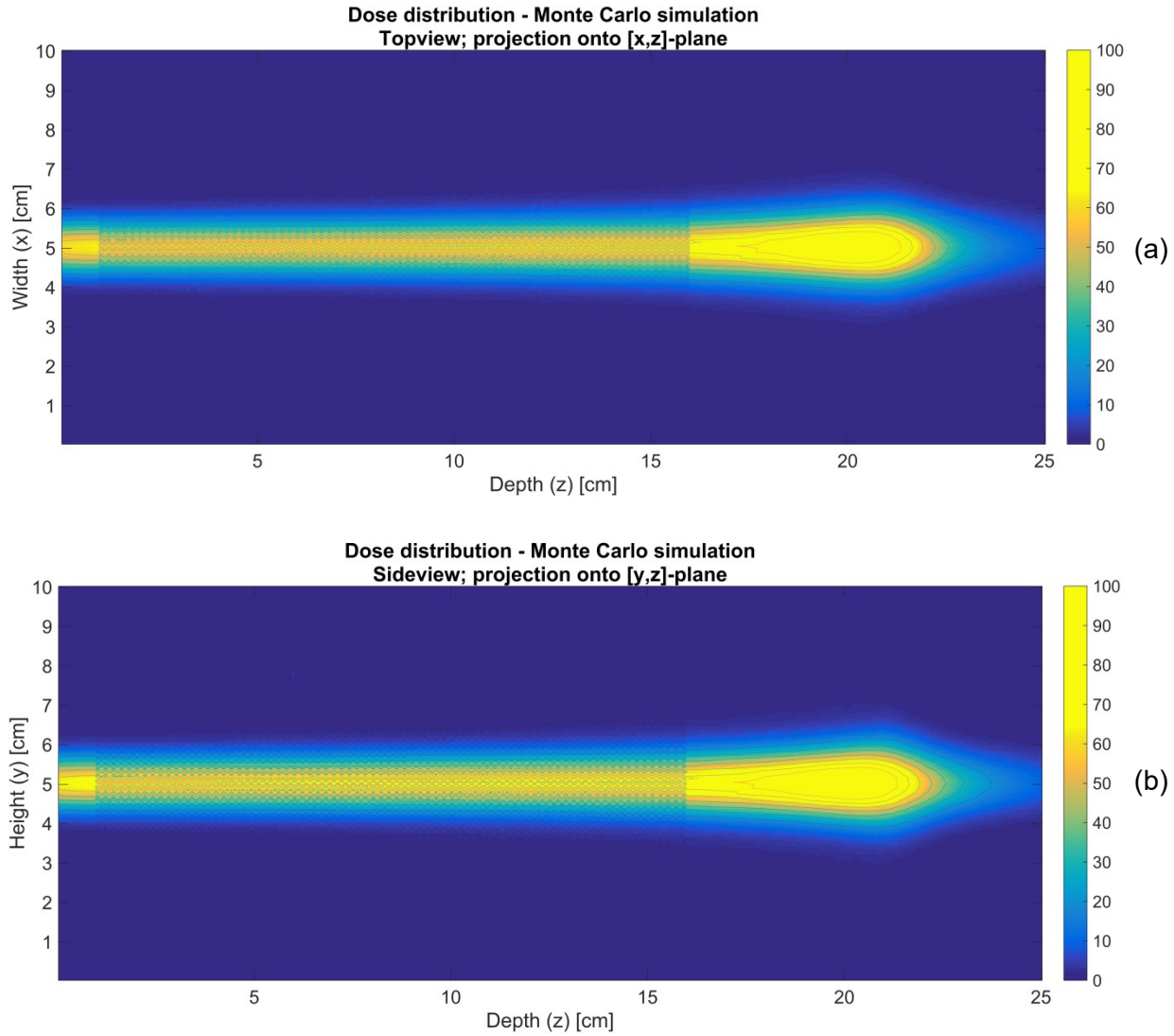

Figure 25, Normalised isodose distribution in a porous structure direct built in TOPAS MC, with cylinders r=0.5mm, for protons of 160MeV. (a) Dose projection onto the [x,z]-plane, (b) dose projection onto the [y,z]-plane.

Figure 25 show the normalised isodose distributions for the porous structures directly built in TOPAS MC. As also shown in the normalised dose distribution in Figure 24, there is a clear elongation of the tail of the Bragg peak. Also, the small cylinders vaguely show, yet are not as pronounced as the larger cylinders for the bilayer case presented in Figure 21, but they do show a lowering of the delivered dose. The isodose profiles for the larger cylinder sizes are

not shown, since these follow a similar distribution as shown here, with the exception that the tail end follows a sharper fall-off, as also presented in Figure 24.

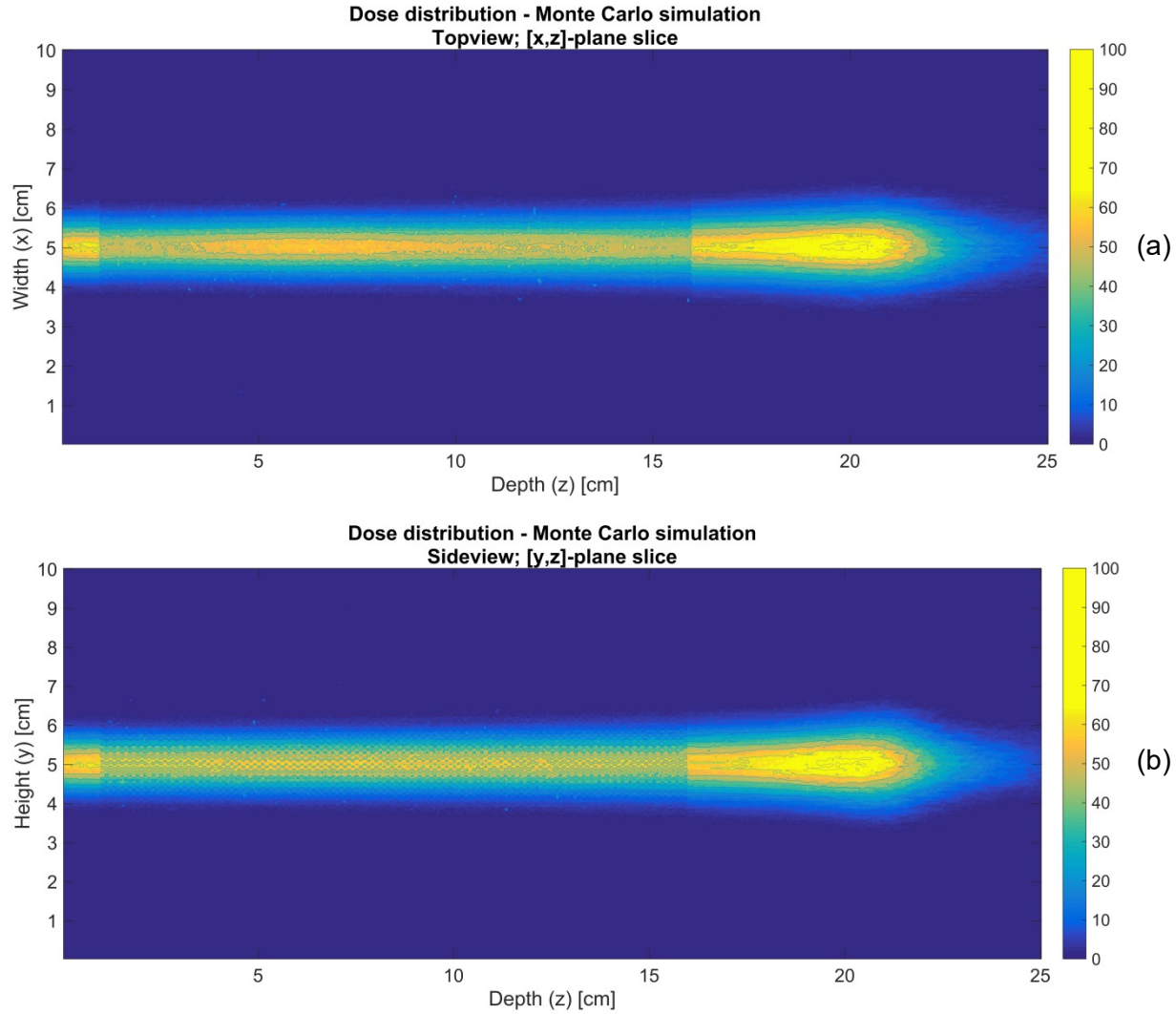

Figure 26, Normalised isodose distribution a porous structure direct built in TOPAS MC, with cylinders r=0.5mm, for protons of 160MeV. (a) Dose sliced onto the [x,z]-plane at y=5cm, (b) dose sliced onto the [y,z]-plane at x=5cm.

The same holds for the in Figure 26 presented normalised isodose distributions. These slices do not show the cylindrical shape clearly, but a lowering of the dose in the porous structure is visible. Again, the other porosities are not shown since they follow a similar pattern.

As was already shown in Figure 23, the dose distribution for the simulation done on the tessellated structure with cylinders of r=0.5mm, shows the largest discrepancy with the other doses. This also shows in the isodose distributions presented in Figure 27 and Figure 28, respectively the projected dose and dose slice.

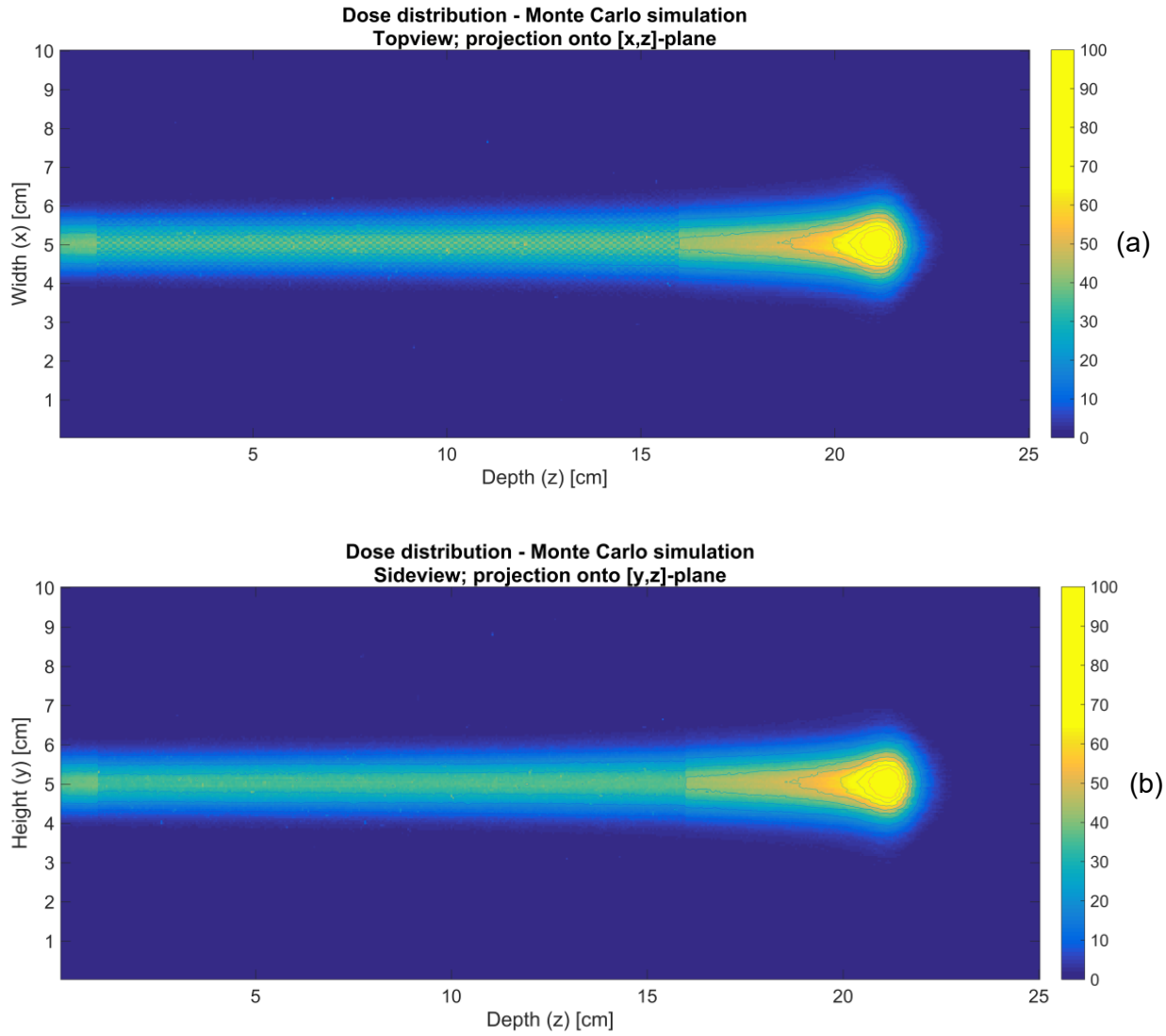

Figure 27, Normalised isodose distribution in a porous structure from tessellated structures, with cylinders r=0.5mm, for protons of 160MeV. (a) Dose projection onto the [x,z]-plane, (b) dose projection onto the [y,z]-plane.

From Figure 27, it shows that the porosity is not visible anymore, nor is there a significant elongation of the Bragg peak tail. An even more distinct difference can be seen in Figure 28, which shows the dose slices. Both plane slices show the individual tracks more clearly than in any of the other isodose distributions. Furthermore, as Figure 28(b) shows, there is very little dose at all in the vertical plane at x=5cm.

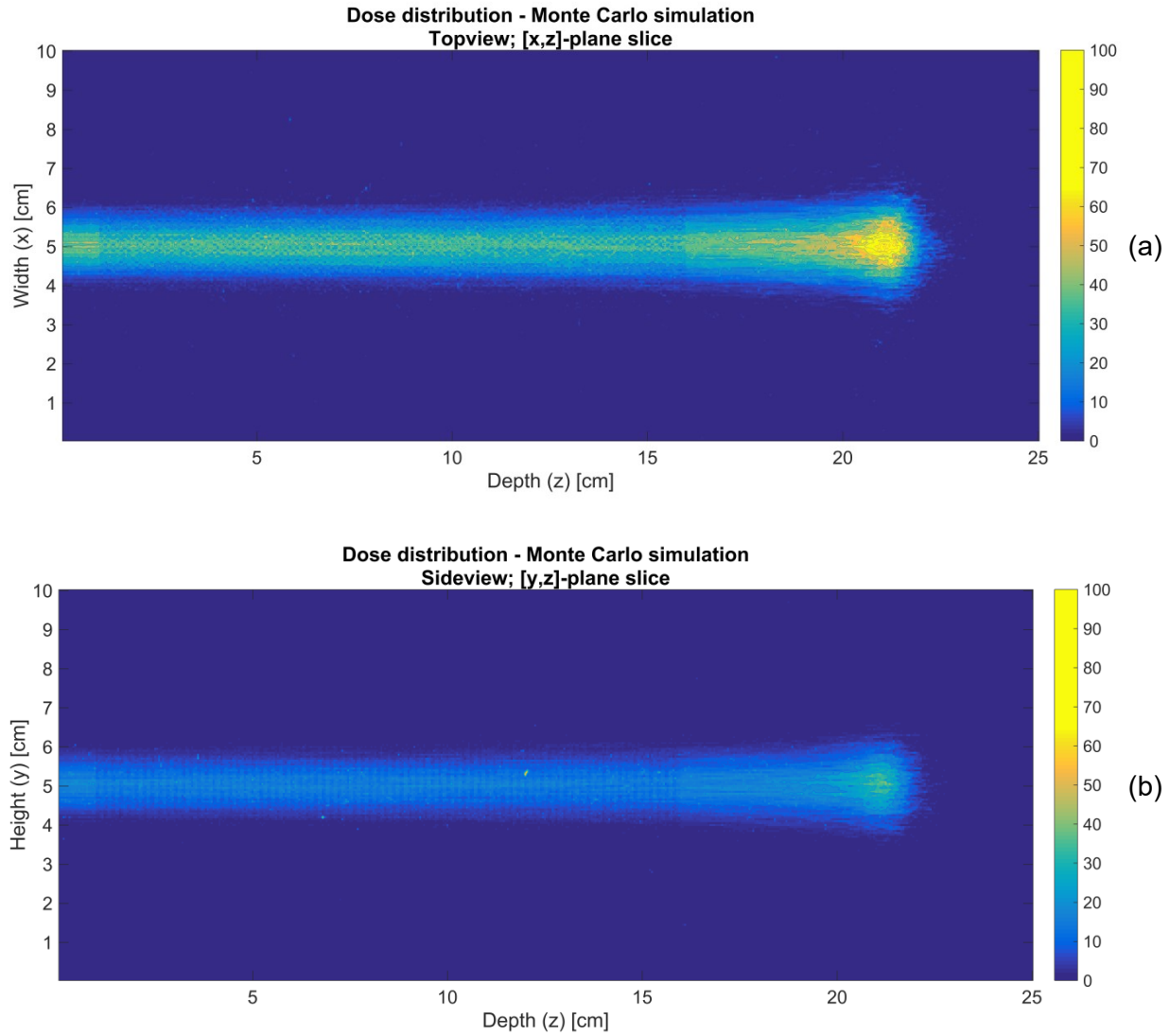

Figure 28, Normalised isodose distribution in a porous structure from tessellated structures, with cylinders r=0.5mm, for protons of 160MeV. (a) Dose sliced onto the [x,z]-plane at y=5cm, (b) dose sliced onto the [y,z]-plane at x=5cm.

Porous, E=120MeV

The normalised dose to medium for proton beams with 160MeV are shown in Figure 29 and Figure 30 for simulations on tessellated structures and direct builds in TOPAS MC respectively. For the simulations performed on the tessellated structures the same should be noted as for the simulations at 160MeV. In order to reduce the required simulating time, the simulation with the smallest porosity (r=0.5mm) was performed with only $1.2 \cdot 10^6$ protons. Furthermore, with this smallest porosity simulation a lot of tracks were removed from the simulation by TOPAS MC, due to simulation errors.

Again, from both figures, it can also clearly be seen that the introduction of porosity causes the Bragg peak to have a significant translation in the direction the proton beam travels. Also, just like in the case with the bilayers, the Bragg peaks become both lower and are broadened.

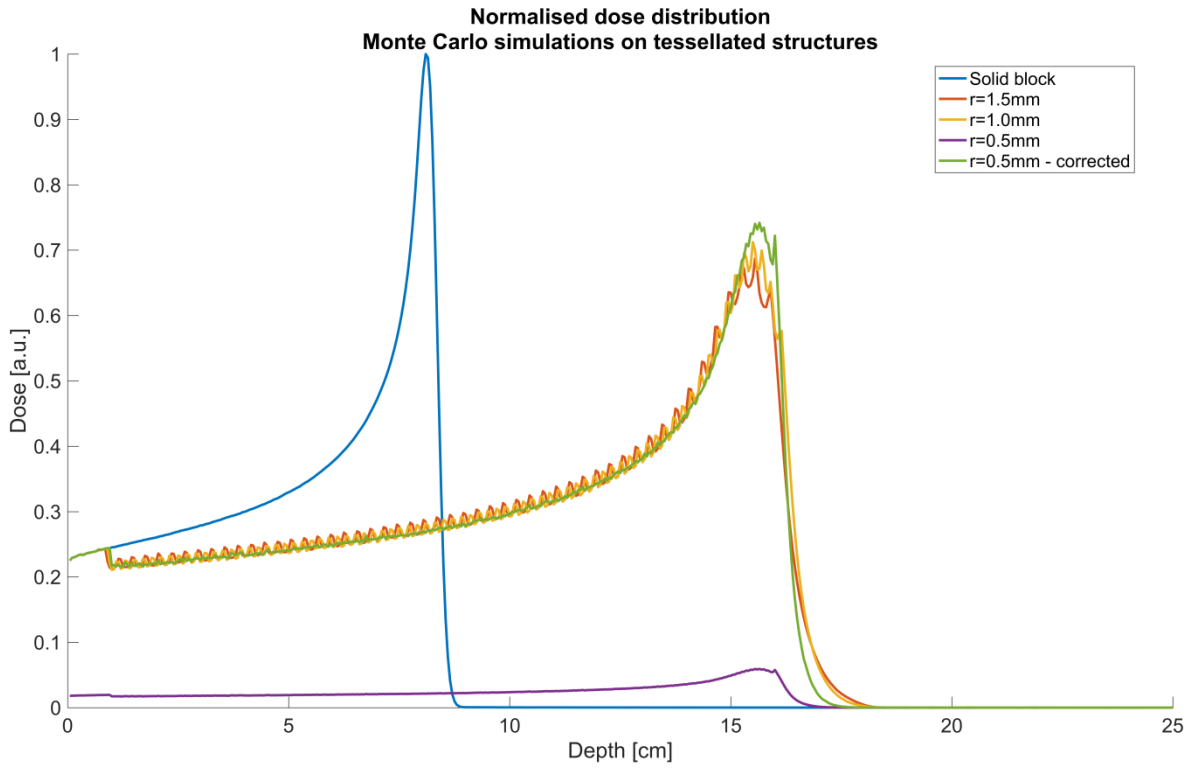

Figure 29, Normalised dose to the medium, in a solid block PVA and porous structures from tessellated structures, with r=1.5mm, r=1.0mm, r=0.5mm, for proton beams with energy 120MeV. The dose is normalised to the dose by the protons in the solid block and determined as the dose in an entire slice.

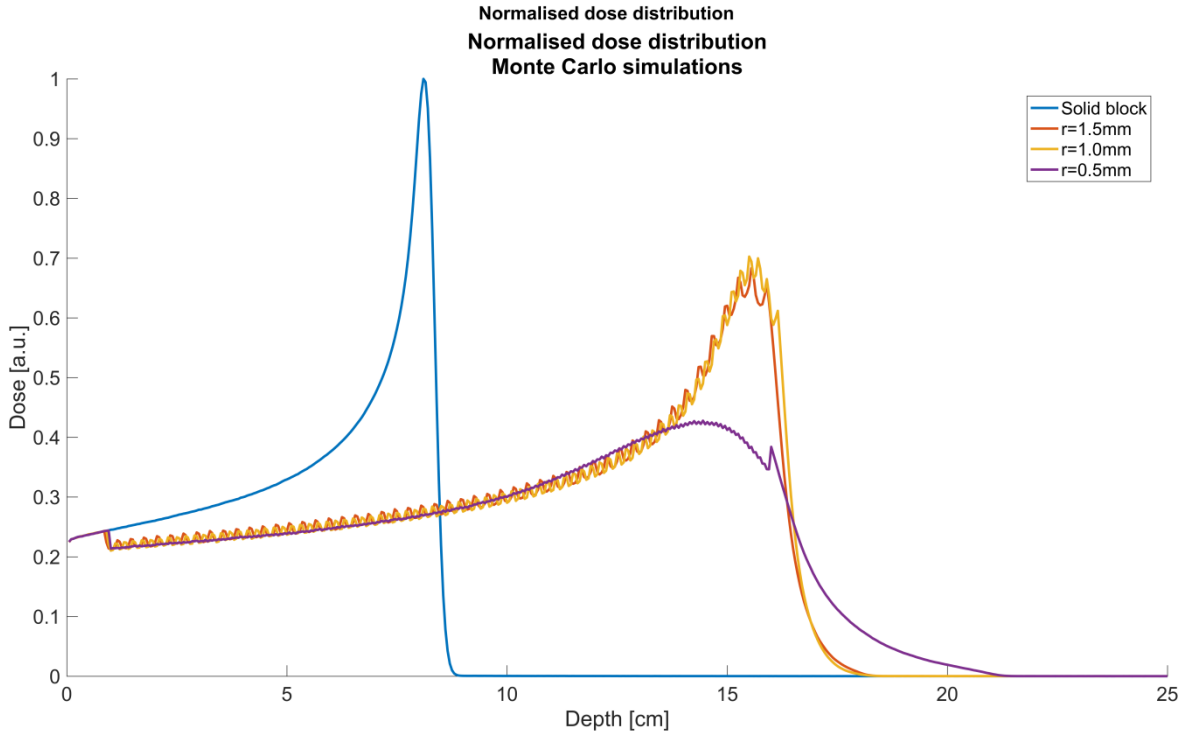

Figure 30, Normalised dose to the medium, in a solid block PVA and porous structures direct built in TOPAS MC, with r=1.5mm, r=1.0mm, r=0.5mm, for proton beams with energy 120MeV. The dose is normalised to the dose by the protons in the solid block and determined as the dose in an entire slice.

Furthermore, also for energies of 120MeV, it can be observed that for both the simulations on tessellated structures as on direct builds in TOPAS MC, the dose distributions for r=1.5mm and r=1.0mm show identical trends, which can also be seen from the near identical numerical values for these dose deposition profiles in Table 6. Also, the characteristic shape of the Bragg peak is still distinguishable from both figures, yet it does show that the Bragg peak is located at the end of the porous section, therefore showing a jagged peak.

Table 6, Numerical values for the porous structues, for proton beams with energy 120MeV, as shown in Figure 29 and Figure 30.

	Bragg peak location [mm]	Normalised dose Bragg peak [a.u.]	80% dose point [mm]	50% dose point [mm]	1% dose point [mm]	FW80M [mm]	FWHM [mm]	Tail length [mm]
Solid PVA	81	1	82.78	83.87	87.50	4.05	12.19	6.5
r=1.5mm	155.5	0.683	160.53	162.90	179.81	14.33	41.37	24.31
r=1.5mm .stl	155.5	0.687	160.16	162.49	179.09	14.07	41.15	23.59
r=1.0mm	155	0.703	161.98	163.96	177.92	13.47	39.45	22.92
r=1.0mm .stl	155	0.712	160.28	163.51	177.21	11.97	38.94	22.21
r=0.5mm	144.5	0.428	161.62	167.05	209.85	46.61	156.84	65.35
r=0.5mm .stl	156.5	0.059	160.94	162.44	172.10	11.75	34.95	15.60

Table 7, Shift and widening of the Bragg peaks in porous structures compared to solid PVA, for proton beams with energy 120MeV.

	Bragg peak shift [mm]	Relative range	FW80M widening	FWHM widening	FWHM/R	Tail lengthening
r=1.5mm	74.5	1.920	3.538	3.394	0.266	3.740
r=1.5mm .stl	74.5	1.920	3.474	3.376	0.265	3.629
r=1.0mm	74	1.914	3.326	3.236	0.255	3.526
r=1.0mm .stl	74	1.914	2.956	3.194	0.251	3.417
r=0.5mm	63.5	1.784	11.509	12.866	1.085	10.054
r=0.5mm .stl	75.5	1.932	2.901	2.867	0.223	2.4000

The correction on the normalised dose for the 120MeV protons is done in the same way as for the 160MeV protons, again all values are the same as the non-corrected values, except for the Normalised dose in the Bragg peak, which becomes 0.742 a.u.. Furthermore, the

FWHM/R ratio for the protons in solid PVA is 0.150. Table 7 also shows, when disregarding the simulation with tessellated structures with r=0.5mm, for all simulations the relative range is almost identical. However, just like with the 160MeV proton beams, the FW80M, FWHM, Tail lengthening and FWHM/R ratio are larger for larger cylinders.

As can be seen from Figure 29, Figure 30 and Table 6, all proton beam dose distributions follow a similar pattern independent of the size of the cylinders, except for the simulation on the tessellated porous structure with cylinders of r=0.5mm. Therefore, since all these simulations follow the same trend, only one case will be displayed. Also, the r=0.5mm cylinders directly built in TOPAS MC shows a similar trend as the dose distribution for the 160MeV protons, with a lower peak dose and a longer tail length than is the case with the larger cylinders.

From Figure 31, it can be seen that the dose distribution is smoothed in the porous segment and that, just like in at a proton beam energy of 160MeV shown in Figure 25, the cylinders are no longer clearly visible. Also, it can be seen that the edge of the porous segment is at 16cm into the block, as there the isodose shows a straight cut-off.

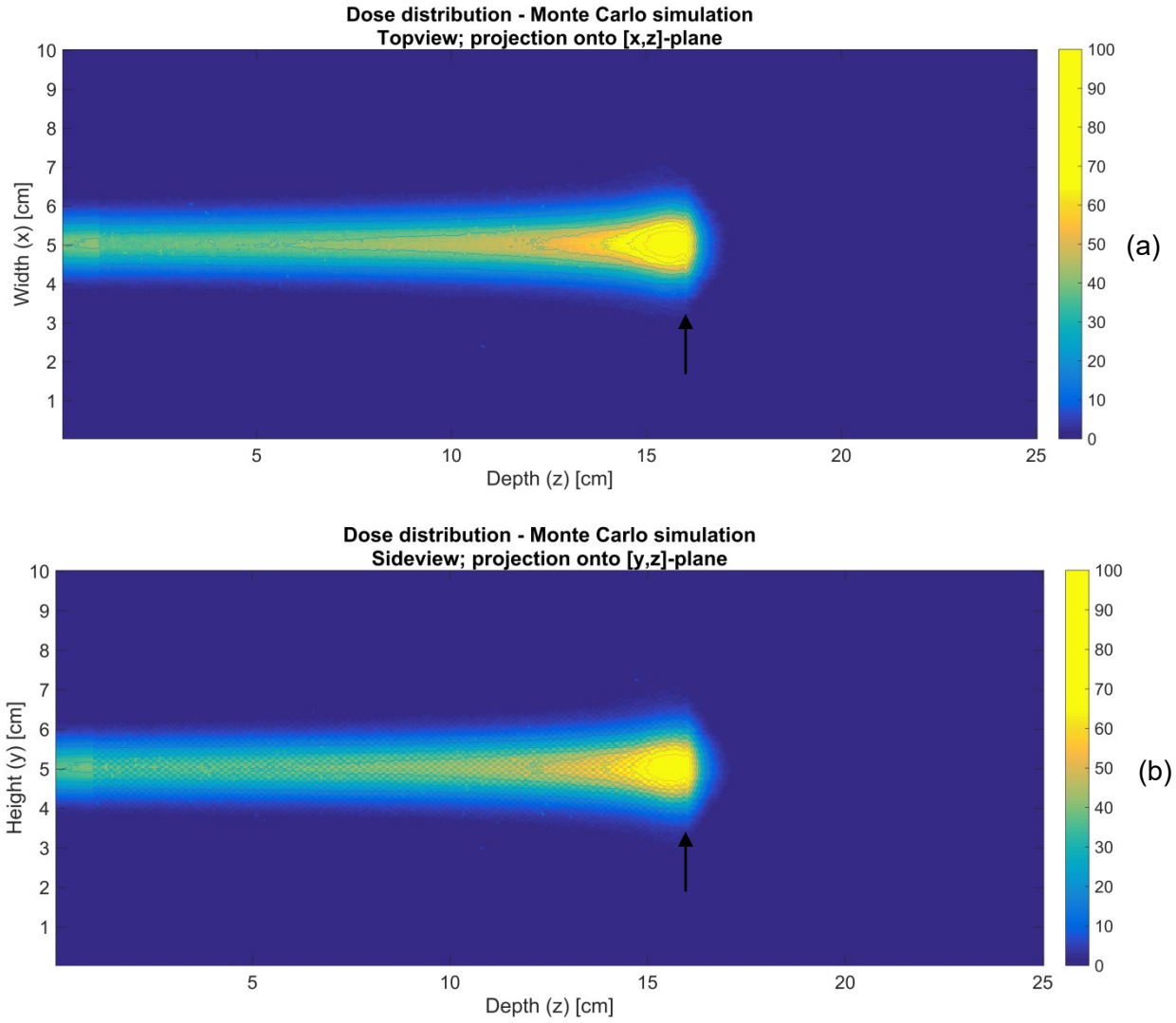

Figure 31, Normalised isodose distribution in a porous structures from tessellated structures, with cylinders r=0.5mm, for protons of 120MeV. The arrows indicate the edge of the porous segment. (a) Dose projection onto the [x,z]-plane, (b) dose projection onto the [y,z]-plane.

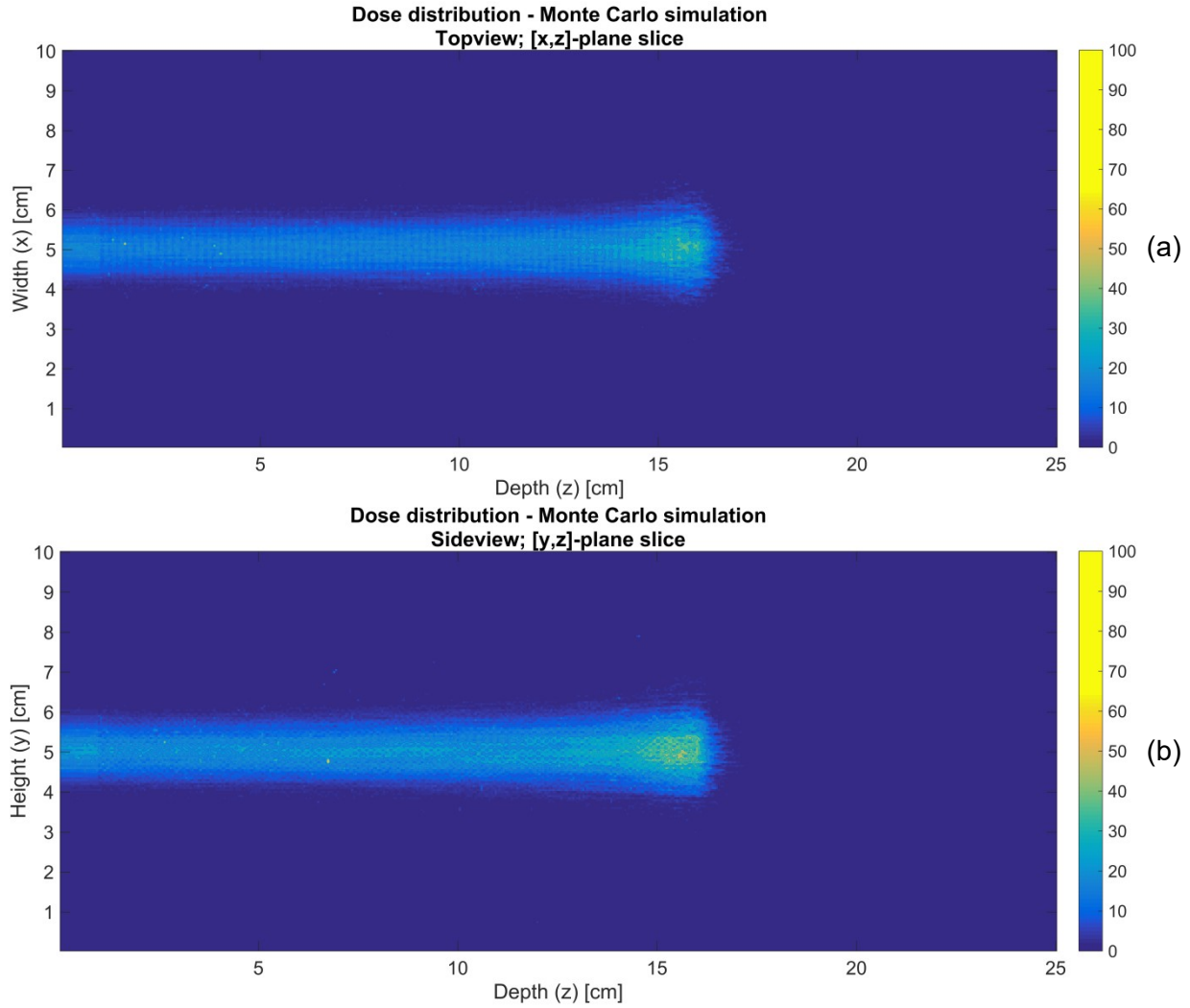

Figure 32, Normalised isodose distribution in a porous structure from tessellated structures, with cylinders r=0.5mm, for protons of 120MeV. (a) Dose sliced onto the [x,z]-plane at y=5cm, (b) dose sliced onto the [y,z]-plane at x=5cm.

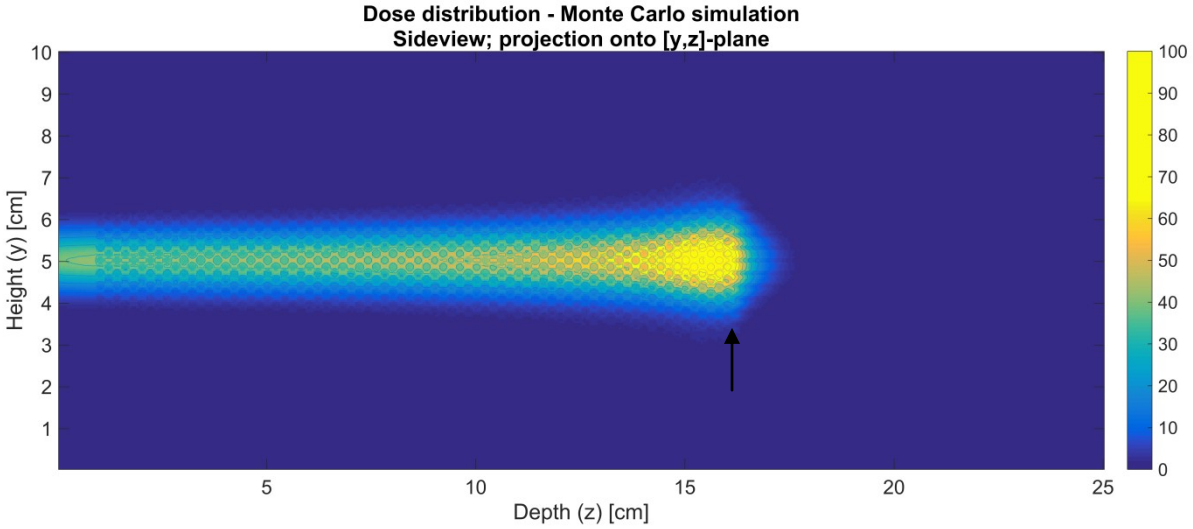

Figure 33, Side view of a normalised isodose distribution in a porous structure direct built in TOPAS MC, with cylinders r=1.0mm, for protons of 120MeV. The arrow indicates the edge of the porous segment.

Furthermore, just like shown in Figure 28 for 160MeV protons, Figure 32 shows that there is little dosage in the tessellated structure in a single slice. Here the individual tracks of protons are clearly visible, especially around the Bragg peak location.

From Figure 33, it shows that the last row cylinders influence the shape of the tail of the Bragg peak, as the tail becomes comb shaped. Also, since these cylinders are twice as large as the cylinders in Figure 31, they show more clearly.

Porous, E=80MeV

The normalised dose to medium for proton beams with 80MeV are shown in Figure 34 and Figure 35, for simulations on tessellated structures and direct builds in TOPAS MC respectively. Again, it should be noted that the simulation on tessellated structures with cylinders of r=0.5mm, the dose distribution is far different than the other dose profiles. This again is due to the earlier stated simulation errors in TOPAS MC, leading to complete proton tracks to be discarded.

Again, from both figures, it can also clearly be seen that the introduction of porosity causes the Bragg peak to have a significant translation in the direction the proton beam travels. Also, just like in the case with the bilayers and the higher energy porous structures, the Bragg peaks become both lower and are broadened.

Furthermore, like for energies of 120MeV and 160MeV, it can be observed that for both the simulations on tessellated structures as on direct builds in TOPAS MC, the dose distributions for r=1.5mm and r=1.0mm show identical trends, which can also be seen from the near identical numerical values for these dose deposition profiles in Table 8. Again, due to the identical nature of all simulations, except for the simulation on the tessellated porous structure with cylinders of r=0.5mm, only one set of isodose distributions will be presented.

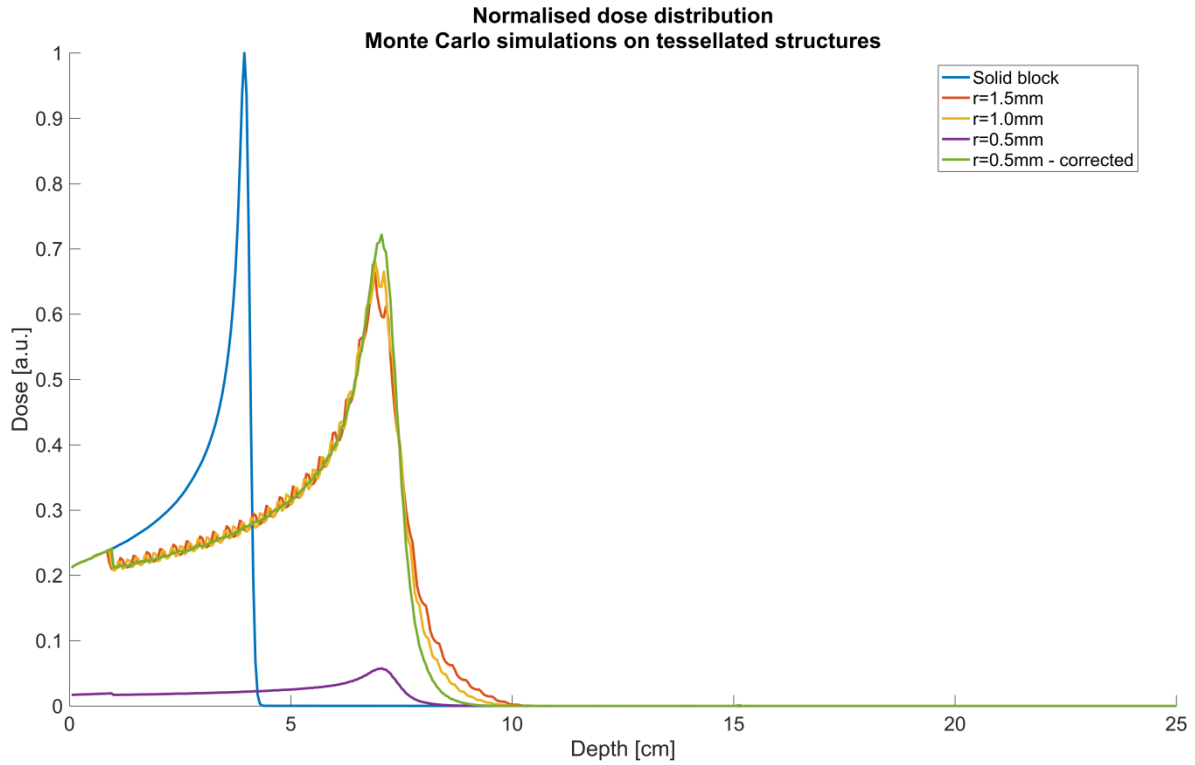

Figure 34, Normalised dose to the medium, in a solid block PVA and porous structures from tessellated structures, with r=1.5mm, r=1.0mm, r=0.5mm, for proton beams with energy 80MeV. The dose is normalised to the dose by the protons in the solid block and determined as the dose in an entire slice.

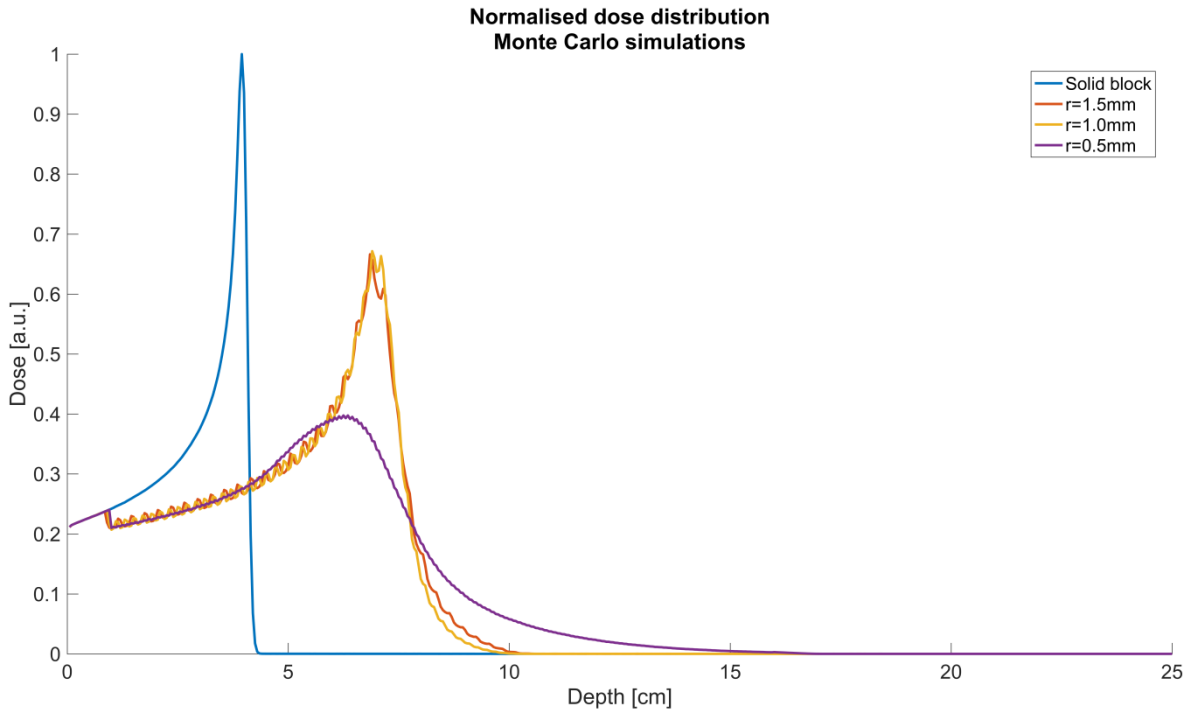

Figure 35, Normalised dose to the medium, in a solid block PVA and porous structures direct built in TOPAS MC, with r=1.5mm, r=1.0mm, r=0.5mm, for proton beams with energy 120MeV. The dose is normalised to the dose by the protons in the solid block and determined as the dose in an entire slice.

Also, the characteristic shape of the Bragg peak is still distinguishable from both Figure 34 and Figure 35, yet it is clearly visible that the Bragg peak is located inside the porous section, therefore showing both jagged peak and tail end.

Table 8, Numerical values for the porous structues, for proton beams with energy 80MeV, as shown in Figure 34 and Figure 35.

	Bragg peak location [mm]	Normalised dose Bragg peak [a.u.]	80% dose point [mm]	50% dose point [mm]	1% dose point [mm]	FW80M [mm]	FWHM [mm]	Tail length [mm]
Solid PVA	39.5	1	40.31	40.88	42.77	1.98	5.82	3.27
r=1.5mm	68.5	0.666	72.65	75.74	98.90	7.37	22.69	30.40
r=1.5mm .stl	68.5	0.676	72.46	75.43	97.74	7.19	22.33	29.24
r=1.0mm	69	0.671	73.14	75.64	94.75	6.98	21.13	25.75
r=1.0mm .stl	69	0.681	72.61	75.36	93.63	6.56	20.79	24.63
r=0.5mm	62.5	0.398	71.69	79.09	152.76	24.45	-	90.26
r=0.5mm .stl	70.5	0.058	72.84	74.84	87.70	6.23	18.3	17.2

Table 9, Shift and widening of the Bragg peaks in porous structures compared to solid PVA, for proton beams with energy 80MeV.

	Bragg peak shift [mm]	Relative range	FW80M widening	FWHM widening	FWHM/R	Tail lengthening
r=1.5mm	29	1.734	3.722	3.899	0.331	9.297
r=1.5mm .stl	29	1.734	3.631	3.837	0.326	8.942
r=1.0mm	29.5	1.747	3.525	3.631	0.306	7.875
r=1.0mm .stl	29.5	1.747	3.313	3.572	0.301	7.532
r=0.5mm	23	1.582	12.348	-	-	27.602
r=0.5mm .stl	31	1.785	3.146	3.144	0.260	5.260

From Figure 35 it shows that the dose for porous structures with r=0.5mm shows that the dose at the entry point is not below 50% of the dose in the Bragg peak, thus a FWHM cannot be determined for this simulation. Furthermore, it shows a very long tail end of the dose, similar to the dose distribution for protons of 160MeV.

The correction on the normalised dose for the 80MeV protons is done identical to the correction for the other energies. Again all values are the same as the non-corrected values, except for the Normalised dose in the Bragg peak, which becomes 0.722 a.u.. Furthermore, the FWHM/R ratio for the protons in solid PVA is 0.147.

It can be seen from Table 9, again when not taking the simulation with tessellated structures with r=0.5mm into account, for all simulations the relative range is almost identical. Also, similar to both other energies, the FW80M, FWHM, Tail lengthening and FWHM/R ratio are larger for larger cylinders.

From Figure 36, the same elongation of the tail end of the Bragg peak becomes visible as from Figure 34 and Figure 35, and has similar comb shape like the 120MeV proton beam isodose distribution shows in Figure 33. Also, whereas the side view projection shows clearly where the cylinders are located, the top view projection creates a seemingly undisturbed Bragg peak dose distribution. This top view does have major disturbances in the individual layers, as can be seen from Figure 37, in the slice through the [x,z]-plane at y=5cm. Here, the individual cylindrical inserts show a distinct lowering of the dose, creating a wave pattern in the isodose distribution.

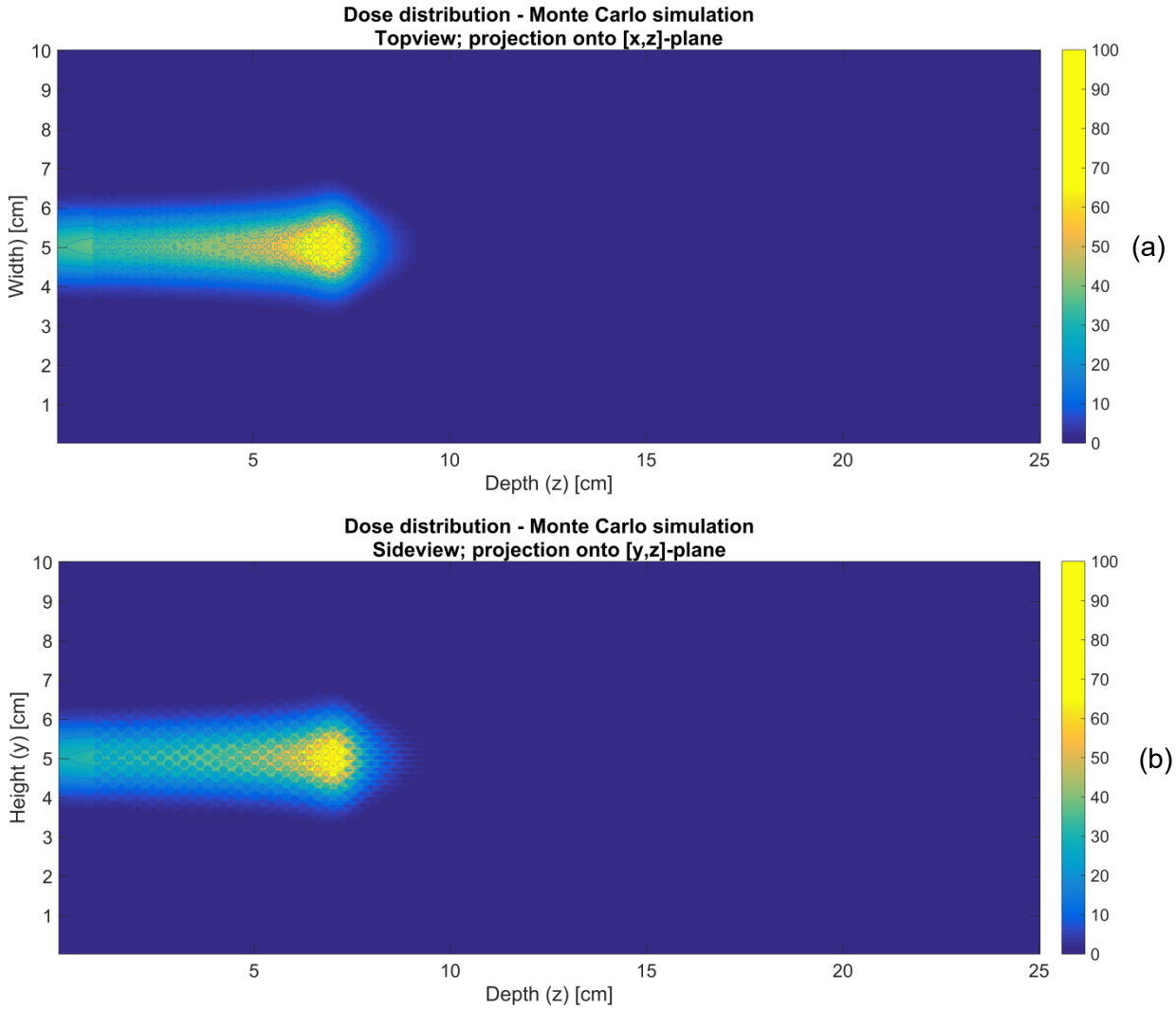

Figure 36, Normalised isodose distribution in a porous structures from tessellated structures, with cylinders r=0.5mm, for protons of 80MeV. (a) Dose projection onto the [x,z]-plane, (b) dose projection onto the [y,z]-plane.

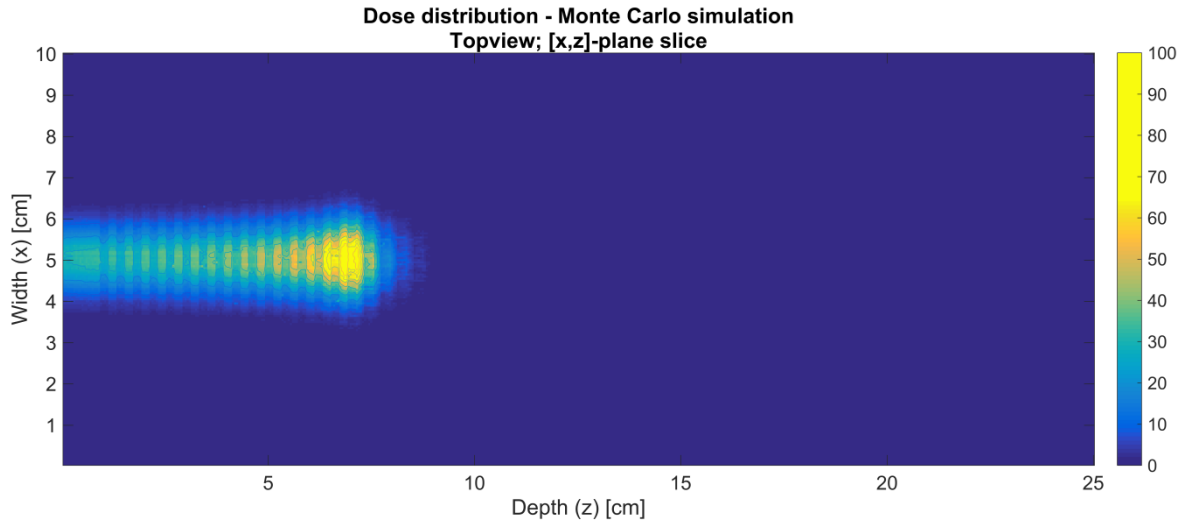

Figure 37, Normalised isodose distribution in a porous structure from tessellated structures, with cylinders r=1.0mm, for protons of 80MeV. Dose sliced onto the [x,z]-plane at y=5cm.

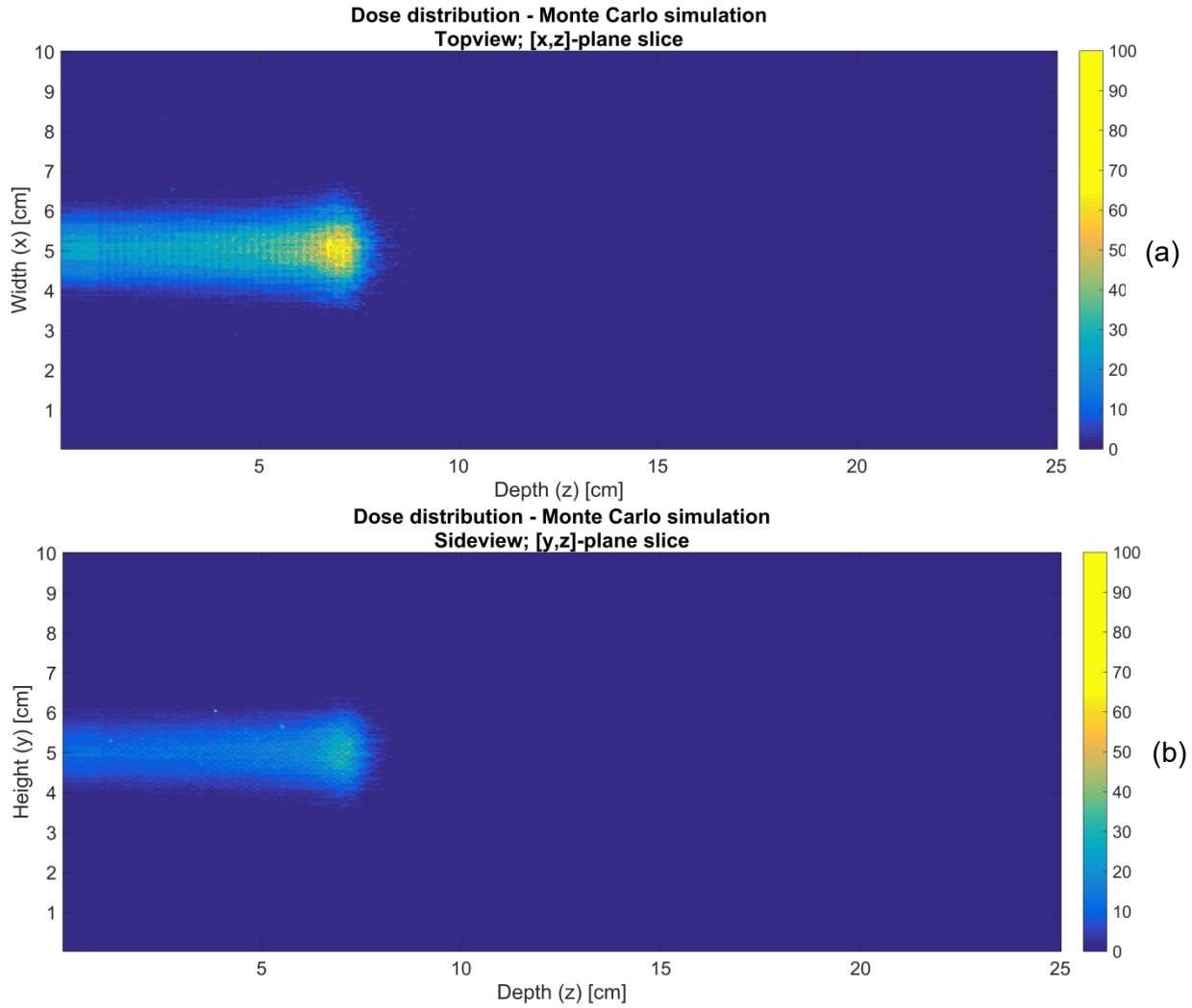

Figure 38, Normalised isodose distribution in a porous structure from tessellated structures, with cylinders r=0.5mm, for protons of 80MeV. (a) Dose sliced onto the [x,z]-plane at y=5cm, (b) dose sliced onto the [y,z]-plane at x=5cm

As was the case for the other proton beam energies, the isodose distribution in a single plane for a proton beam with 80MeV per proton, as shown in Figure 38, the individual proton tracks are visible. Also, the structure of the porosity can vaguely be distinguished.

Adjusted density

The normalised dose distribution for the density adjusted PVA, is compared to that of both the solid block of regular PVA and to the porous block on which it the adjusted density is based. Two comparisons are shown in Figure 39 and Figure 40.

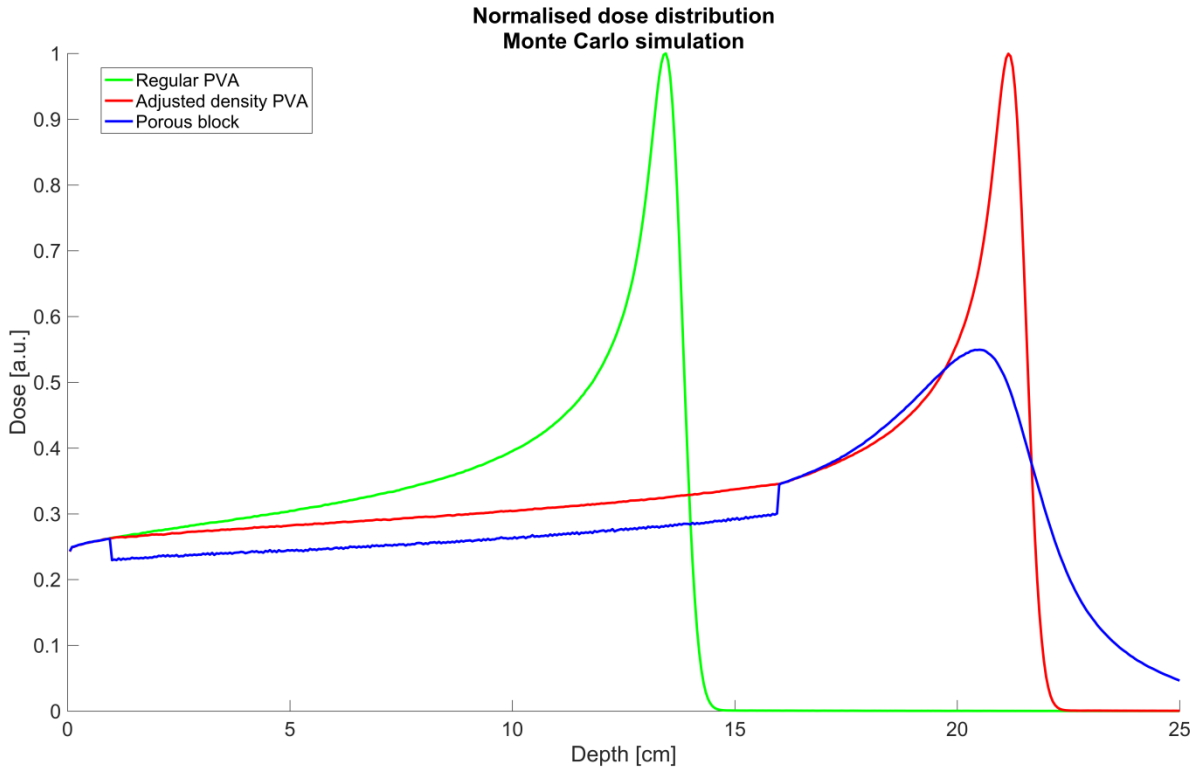

Figure 39, Normalised dose to medium, in a solid block of regular PVA, a solid block of PVA with adjusted density and porous structures directly built in TOPAS MC, with r=0.5mm, for proton beams with energy 160MeV. The dose is normalised to the dose by the protons in the regular PVA and determined as the dose in an entire slice.

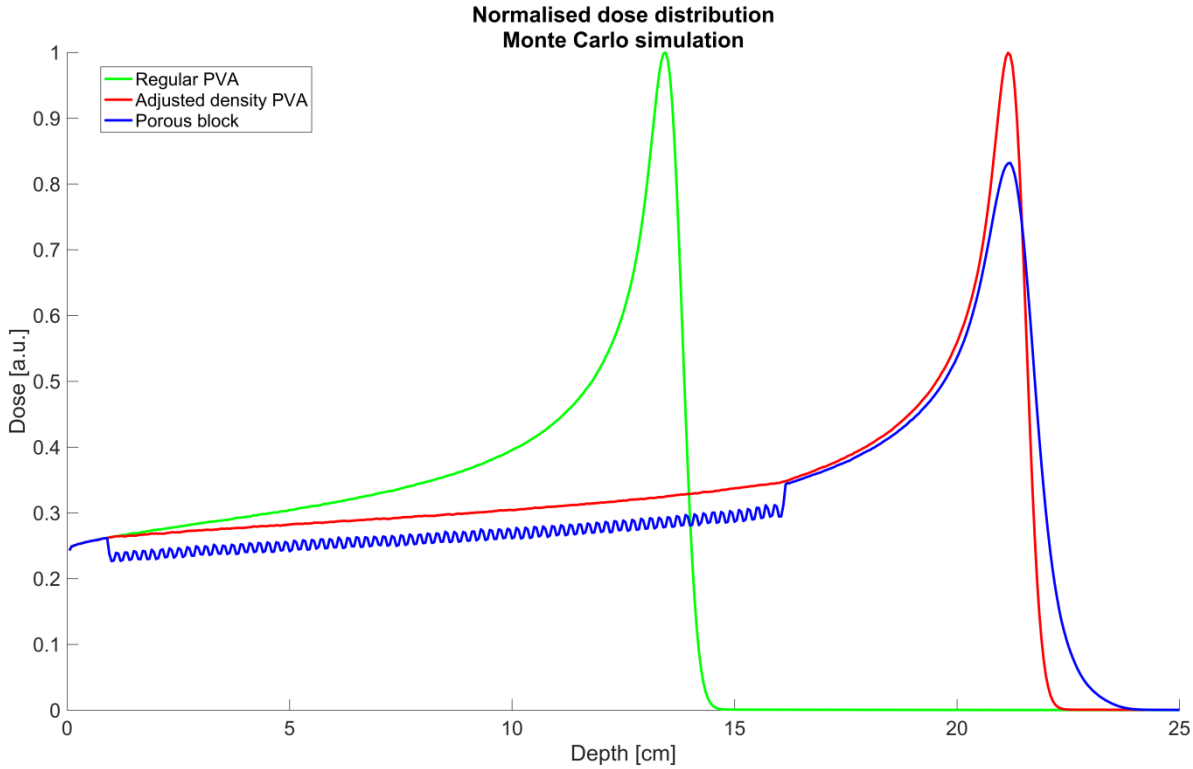

Figure 40, Normalised dose to medium, in a solid block of regular PVA, a solid block of PVA with adjusted density and porous structures directly built in TOPAS MC, with r=1.0mm, for proton beams with energy 160MeV. The dose is normalised to the dose by the protons in the regular PVA and determined as the dose in an entire slice.

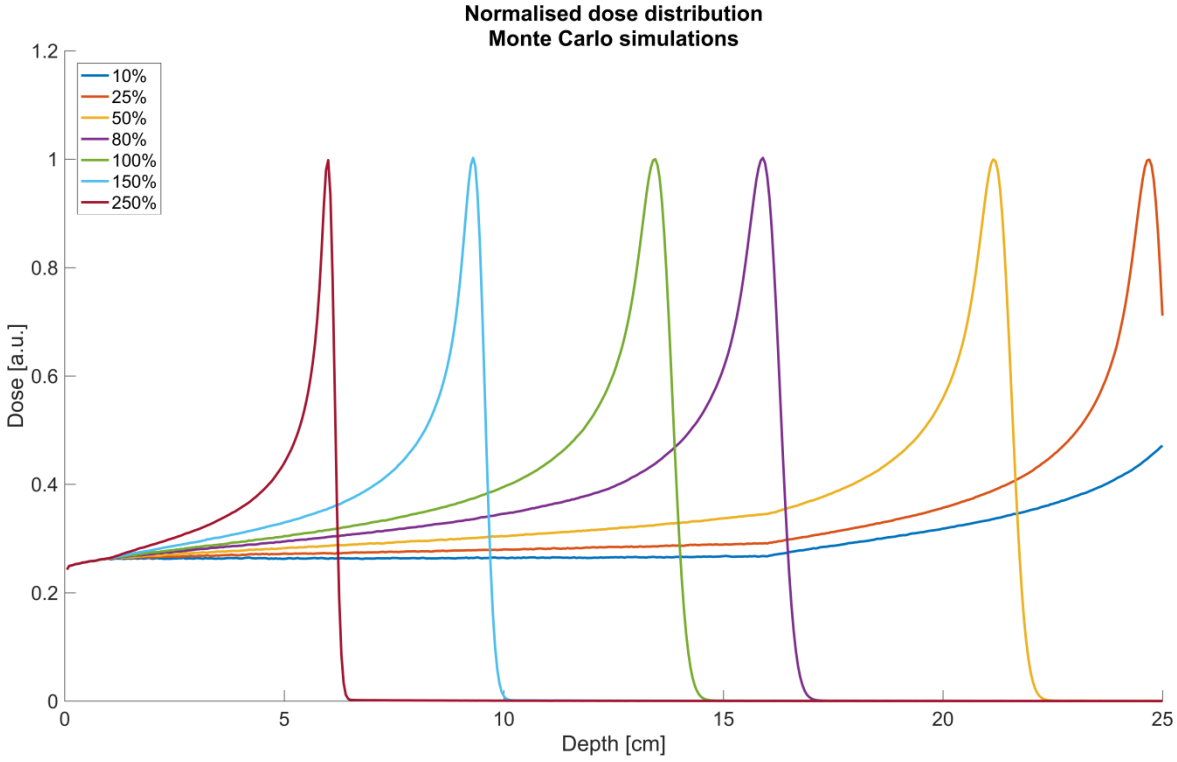

Figure 41, Normalised dose to medium in density adjusted PVA blocks, from 10% to 250% regular density, for proton beams with energy 160MeV. The dose is normalised to the dose by the protons in the regular PVA and determined as the dose in an entire slice.

As was shown in Figure 24, the dose distribution for the porous block from the tessellated structure with cylinders of r=0.5mm, differs from the other dose distributions. This is no different in the comparison to the adjusted density PVA, as is displayed in Figure 39. The in Figure 40 displayed comparison between adjust density PVA, regular PVA and the porous structure the density was adjusted to. The other density adjusted PVA dose distributions follow this same trend, hence will not all be separately presented.

It can be seen from Figure 41 that all dose distributions still show their characteristic Bragg peak shape, and that all have an identical peak dose. Also, there are two discontinuity visible, at 1 cm and at 16cm. At the discontinuity at 1cm, it shows that the steepness of the dose delivery curve is lower for a lower adjusted density, thus less dose is delivered to the medium. The discontinuity at 16cm is only distinguishable for the lowest three densities. Lastly, the Bragg peak for the lowest density PVA does not show, since these protons were not slowed down enough in the adjusted density segment to be able to be completely stopped in the PVA block.

Figure 42 shows the isodose distribution for the PVA density adjusted to the same average density of the porous PVA for cylinders of r=0.5mm. Since this block is rotationally symmetric, only the side view is presented. From this figure, the dimensions of the density adjusted segment cannot be discerned, the only indication that the distribution shown in this figure is not from a homogeneous block of regular PVA, is the fact that the hot spot from this pencil beam is at a depth of approximately 16cm into the block instead of the 14cm for the dose deposition of proton beam in homogeneous PVA, as shown in Figure 18.

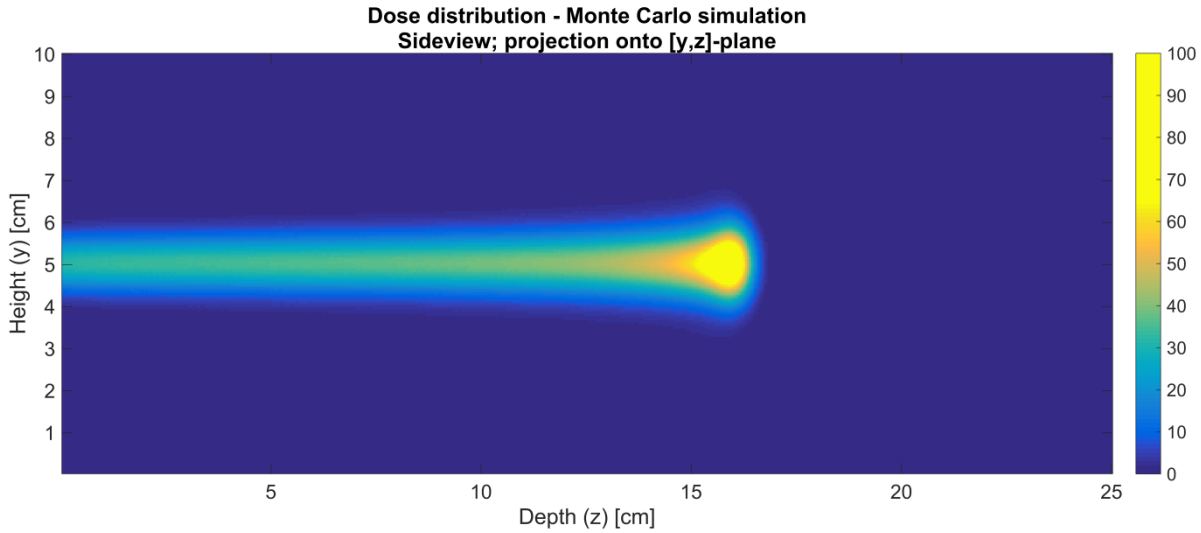

Figure 42, Side view of the normalised isodose distribution in a PVA block with an adjusted density segment, for protons with energy 160MeV.

Discussion

As shown with the sample prints from the Ultimaker3 printer in Figure 16, there are significant malformations in the prints. The left-hand side object in the figure was designed to have straight edges, however the top layer of this object clearly shows undulations. The object on the right of the figure shows the inability of this printer to create objects which have a significant overhanging structure. Therefore it can be concluded that this printer is not able to print at the accuracy level desired to create a phantom that closely resembles heterogeneous tissues, which has lead to the decision to discontinue the use of the Ultimaker3 as an AM device. Furthermore was, as mentioned before, the Form2 printer not subjected to a similar test as the Ultimaker3, but the choice was made to follow the specifications as provided by the producer, as a basis for the dimensions of the cylinders in the porous structures.

Monte Carlo simulations

For all three energy levels, the simulations performed on the tessellated structures with cylinders of r=0.5mm, show a completely different dose distribution compared to the other cylinder sizes and to the similar structure directly built in TOPAS MC, as shown in Figure 23, Figure 29 and Figure 34. This also clearly shows in Table 4, Table 8 and Table 8. All three tables show that the normalised dose is an order of magnitude lower than that of the simulations that were built directly in TOPAS MC. The lowered dose distribution and shape of the distribution can all be attributed to the fact that these simulations, due to their extreme long duration, were performed with a lowered total amount of protons and a very significant number of tracks resulted in errors, as also shown by the visible particle tracks in Figure 28, Figure 32 and Figure 38. Therefore, the as shown in Figure 23, Figure 29 and Figure 34, the dose as a result from the successful proton events has been corrected to correspond to the $1.5 \bullet 10^6$ protons that the other simulations are performed with.

A possible explanation for these errors is the fact that the ability to load tessellated structures in TOPAS MC is a fairly new feature, therefore still being subject to issues. It could for instance be that the simulation software has difficulties with boundary layers between air and PVA when it concerns tessellated structures.

This discarding of proton tracks leads to specific paths through the material to not contribute to the dose distributions as a whole, which in turn means that these simulations may not be an accurate resemblance of the dose that actually would be delivered. Therefore the three erroneous simulations will not be discussed in further, since these show too many errors during the simulation, and will only be compared in their to $1.5 \bullet 10^6$ protons corrected form.

Bilayer

Figure 20 shows a clear dip in the dose to the medium at 10mm, were the bilayers are located. The lowered dose follows a circular pattern, as is to be expected from a cylindrical air cavity. Furthermore, the Bragg peak shows a translation in the beam direction as a consequence of the bilayer. The same holds true for the 80%, 50% and 1% dose points of all bilayer blocks. This translation of all four of these points is equal to twice the radius of one

cylinder, for which the most logical explanation is that in the air filled cylinders little dose is delivered, the protons pass through almost unobstructed, which in itself is also the explanation for the lowering of the dose in the bilayer location. The fact that there still is some dose at this location, is that the dose shown in Figure 20 is the dose in a whole slice in the depth direction, thus the dose delivered to the PVA around the air filled cylinder prevents the dose to drop to 0Gy. Also, the amount of dose delivered in the peak location shows only a very small drop, with a maximum of 1% less dose delivered in the Bragg peak for the bilayer with the largest cylinders. This lowering of the dosage can be contributed to the fact that the PVA in the bilayer does slow down some of the protons that pass through the material instead of air, therefore slightly less energy can be delivered at the end of the proton beam track.

Just like the dose points, the FW80M, FWHM and tail length show only a very minute increase, which is larger for larger cylinder sizes. This can also be contributed to the fact that the air cavities allow the protons to pass through almost unobstructed. With a larger cylinder, the difference between a path through PVA or air becomes more pronounced, the proton that passes through PVA will be slowed more. Thus the energy spread after the bilayer increases more for larger cylinder sizes, with the aforementioned peak broadening and tail elongation as a result.

This means that the introduction of a bilayer just after the entry point of the proton beam acts like an air barrier, which does not result in a significant shift in dose delivery, but only causes a range extension. This is further exemplified by the isodose distributions that are presented in Figure 21 and Figure 22, which show an isodose distribution in the Bragg peak that have an identical shape as the pristine Bragg peak in solid PVA in Figure 18.

Porous, E=160MeV

From Figure 23, Figure 24 and Table 4, it shows that there is negligible difference between the simulations performed on tessellated structures and those that have been directly built in TOPAS MC. For both r=1.5mm and r=1.0mm cylinders, there is a shift in the Bragg peak location approximately 75mm. This is equivalent to the maximum total length of air through which the protons can travel, since the porous structure in all cases is approximately 150mm long, with, depending on the level at which a straight line is drawn through the porous segment, is up to 50% air. As was shown in the bilayer case, an air cavity acts as a range extender equivalent to the path length through the air, therefore the shift of 75mm is very logical.

A further parallel with the bilayer case can be drawn, since the Bragg peak becomes both lower and is broadened, which also showed in the bilayer case, although not as pronounced as in the porous structures. Just like in the bilayer case, this effect can be attributed to the fact that, due to passing through the porous structure, an energy spread in the proton beam is induced at the back edge of the porous structure. This leads to the protons that have passed through most PVA to deposit their energy closer to the original Bragg peak location for protons that pass through a homogeneous block of PVA, and the protons that pass through up to 50% air to still have more energy after the porous structure, thus travelling further into the block. Furthermore, the tail end of the Bragg peak to become less steep, which is also a direct consequence of this induced energy spread.

When looking at Table 5, it can be seen that the widening of the FW80M and FWHM is between 1.3 and 1.8 times, compared to the homogeneous PVA for all cases, except for the porous structure directly built in TOPAS MC, with cylinders of r=0.5mm. This shows a peak broadening that is close to 5 times, three times more than the other simulations. Again, just like with the bilayers, this widening of the Bragg peak is larger for larger cylinder sizes, since

the energy spread is larger in those cases. The energy spread is larger, since the chance for a proton to travel through a longer path of air also is more pronounced with the larger cylinders. This again can be attributed to the fact that the air in the porous structures allows the protons to pass through almost unobstructed. Even though the average density in the porous segment is the same for all three cylinder radii, with smaller cylinders, a smaller spread in energy can be observed. This can be attributed to the fact that protons have less interactions with air than with the PVA. During this interactions that protons lose energy, but also have a chance to be deflected from their original path and is more pronounced for lower energetic protons. With the larger cylinders, the protons will travel through larger sections of either air or PVA at the time, therefore making the effect also larger.

This also reflects in the FWHM/R ratios, which show that at the largest cylinders the ratio increases compared to that of solid PVA. For the smallest cylinders, it shows a small decrease in this ratio, which also is a direct result of the smaller energy spread for the smallest cylinders. Also, the fact that the ratio decreases is due to the increased range due to the porosity. As Table 4 shows, the absolute width of the Bragg peak is, of course, larger.

This peak broadening also explains the lowering of the peak dose, since the total dose remains the same, since an equal amount of protons is used in all simulations, therefore the total amount of energy that can be deposited is also the same.

When looking at the dose distribution and isodose profiles for porous structures directly built in TOPAS MC with cylinders of r=0.5mm, as shown in Figure 24, Figure 25 and Figure 26, it shows that the dose delivered in the Bragg peak is even more broadened than those of the porous structures with cylinders of larger radii. Furthermore, the normalised dose to medium shows no wave pattern in the porous segment of the block, nor do the isodose profiles show a distinct circular pattern, contrary to that of larger radius cylinders. This could be a result of an artefact due to the scoring grid. This scoring grid has edges that are equal to the radius of the cylinders, therefore every cylinder is perfectly enveloped by 2x2x200 voxels, each having identical volume fractions of PVA and air, since the central axis of the cylinders perfectly coincides with the edges of the scoring voxels. For the larger cylinders, this does not hold, as in these simulations, the volume fractions of PVA and air differ per voxel.

Porous, E=120MeV

From Figure 29, Figure 30 and Table 6, a similar to the 160MeV proton beams negligible difference between the simulations performed on tessellated structures and those that have been directly built in TOPAS MC shows. Also for protons with energies of 120MeV, for both r=1.5mm and r=1.0mm cylinders, there is a shift in the Bragg peak location approximately 75mm. Again, this shift is both logical and can be contributed to the maximum total length of air through which the protons can travel.

For the 120MeV proton beams, Table 7 shows that the peak is also lowered and the FW80M, FWHM and tail length are broadened by 2.9 to 3.5 times. The lowering of the peak dose is greater for 120MeV protons than for 160MeV protons, which is due to the greater broadening of the Bragg peak, as also in these situations, the total dose delivered remains the same, but is smeared out over a longer path length. What is more, the FWHM/R ratio is larger for larger cylinder sizes, just like with the protons of 160MeV, for the same reason. However, with the 120MeV protons this ratio is larger for all cylinder sizes than the ratio for solid PVA. This can be attributed to the Bragg peak being almost completely enveloped by the porous segment of the PVA block, since the energy spread relative to the entrance energy of the protons is larger than that for 160MeV protons.

The greater broadening of the Bragg peak can be attributed to the fact that the relative energy spread at the edge of the porous segment is larger than with 160MeV protons, since the Bragg peak is just located inside the porous segment, thus the protons that travel through the most PVA are completely stopped before being able to exit the porous segment, yet the protons that travel through the most air still have a significant part of their energy. This also shows in the jagged nature of the peak itself, which can also be attributed to the scoring grid, in which some of these scoring voxels envelope a larger fraction of PVA.

In Figure 31 and Figure 33, a line is visible at a depth of 16cm into the block, an indication of the edge of the porous segment. This line is also visible in Figure 29, with the extra tooth in the beginning of the fall-off region of the Bragg peak. At this location, a significant fraction of the protons have lost most of their energy, therefore, when entering the homogeneous PVA section, only have a limited amount of energy available. Since the LET for protons increases with decreasing proton energy, it is logical that these low energetic protons stop very close to this porosity edge. The difference between protons that have passed through mostly air or and those that passed through mostly PVA shows in Figure 33, creating a comb pattern. The figure also shows the edge of the porous segment. This is both due to the visible edge in the isodose distribution and since in this figure the cylinders are clearly visible, since the shown isodose distribution is for a porous structure with cylinders of r=1.0mm. The protons that have travelled through mostly air have more energy remaining and therefore are able to penetrate the homogeneous PVA segment further.

Porous, E=80MeV

For proton beams with energies of 80MeV, as described in Figure 34, Figure 35 and Table 8, also show that there is negligible difference between the simulations performed on tessellated structures and those that have been directly built in TOPAS MC. For both r=1.5mm and r=1.0mm cylinders, the Bragg peak shifts by almost 40mm into the block, therefore is not able to exit the porous segment of the block. This results in a FW80M and FWHM to broaden by a factor of 3.1 to 4, similar to the broadening shown for 120MeV proton beams, an indication that the widening of the Bragg peak in these porous media may be the same for different proton energies, if the Bragg peak is enveloped by the porous segment.

The elongation of the tail lengths is significantly greater in this case, which is up to an order of magnitude longer. Again, this is to be attributed to the protons that have travelled the greatest distance through air, up to 50% of their path length.

This also means that, for proton beams that are to be delivered in media of such heterogeneity, the lateral fall-off can vary greatly with the desired dose fall-off. This is also visible in Figure 36 and Figure 37, as these figures show a great elongation of the fall-off region, which also causes the dose distribution to become more pike shaped.

Adjusted density

From Figure 39, Figure 40 and Figure 41, it shows that introducing a segment of PVA with an adjusted density results in a shift in the Bragg peak location, as to be expected, since the lower density of the material means that there is a lower chance for the proton to have an interaction with the medium, thus the LET of the proton in that segment is less. A higher density of course has the contrary effect, stopping the protons faster. Furthermore, Figure 41 shows two discontinuities in the dose distribution, one at 1cm depth and another at 16cm depth. These discontinuity clearly show the edges of the adjusted density segment, after which the regular PVA density continues.

Also, since the material is homogeneous in each of the individual segments, the Bragg peaks of the proton beams through the adjusted density PVA segments show no disturbance in

Figure 41. However, these dose distributions all show an identical dose delivered to the medium in their respective Bragg peak locations. This is logical, since the higher density PVA has more mass in the adjusted density segment, therefore a larger stopping power. And since the delivered dose is equal to the delivered energy per unit mass, this is to be expected. This also explains why the dose distribution curves flatten in the adjusted density segment for lower densities, since in that segment the lower density does not stop the protons as effectively as the higher densities.

What is more, is that Figure 39 and Figure 40 show that the shift in Bragg peak location is very similar for the adjusted density and porous cases, with the difference that the peak widening and tail elongation is less for the adjusted density.

However, the adjusted density does not show a change in the isodose profile, as shown in Figure 42, in which the isodose profile for a 160MeV proton beam in a block with a 48% density PVA segment is incorporated. The only distinguishable difference with the isodose profile for a similar proton beam through homogeneous, regular density, PVA, is the fact that the hot spot has been shifted just over 2cm deeper into the block. Together with the dose to medium shown in Figure 41, this leads to think that a mistake has occurred in the simulations with adjusted densities.

Conclusions

The results show that 3D printing brings its own challenges at the high level of small details required to accurately print heterogeneous phantoms. The simulations show an analogy in the effect a bilayer and a porous structure in the fact that the air in the cylinders act as a range moderator. Furthermore, within the simulations performed on porous structures, both from tessellated structures and those that were directly built in TOPAS MC, there is a great agreement. Also, simulations performed on blocks with segments of adjusted density PVA show that does influence the location of the Bragg peak, but that there is no conformity with the porous structures.

3D printers

The first build with the Ultimaker3 showed great promise for this printer to be used to create phantoms, however the printer was not able to deliver on this promise. The second and third builds with this printer showed distortions that were too severe for this printer to be reliable in creating structures with a high level of small details. Therefore the use of the Ultimaker3 was discontinued for this research. The second printer, the Form2, was not subjected to a similar set of tests to verify the provided printing specifications. The printing specifications did function as a basis for the size of the available porosity.

Monte Carlo simulations

Since the simulations on both the tessellated structures and directly built in TOPAS MC show near identical results for larger radii, it can be concluded that for further research the simulations are best performed on the structures that are directly built in TOPAS MC. This, since the simulations done one tessellated structures require far more time, which can be as much as requiring over an order of magnitude more total simulation time. This is even though the creation of the simulation world in TOPAS MC takes longer and is more prone to errors than using CAD software, since with CAD software the building of the structure is done visually, contrary to via TOPAS MC. The cause for the total simulation time to be significantly longer, since the both the initialisation and simulation times for tessellated structures are a significantly longer. Furthermore, due to the large number of errors in the simulations performed on tessellated structures with cylinders of r=0.5mm, this is another reason to discard the use of tessellated structures for simulations, unless the simulation software is upgraded such that it is able to properly process the tessellated structure files.

When the proton irradiation is performed on homogeneous tissue which is located after a heterogeneous segment, it is possible to irradiate a tumour with a slightly broadened Bragg peak. The range moderation as a result of the porous structure should carefully be taken into account for this. However, if the Bragg peak is located inside heterogeneous material, the Bragg peak becomes significantly distorted, mostly in the beam direction. This is also due the fact that the porous segment is built from a highly regularised grid of cylinders, therefore

creating specific paths that go through mostly PVA or mostly air, which results also in a more regularised dose distribution pattern.

From the results of the simulations performed on the blocks with adjusted density, it appears that the dose distribution in for the PVA block with a porous segment is in good agreement with a segment of adjusted density, when looking at the shift in Bragg peak location. When looking at the shapes of these two Bragg peaks, it can be seen that there is some more broadening and widening of the peak if the protons travel through a porous material. This means that the adjusted densities can be used as a quick check where the Bragg peak will end up after the porous segment, but are not suitable to be used to determine how the exact shape of the peak will be influenced. It is a quick check, since the simulation times for the adjusted densities are far shorter than those for porous blocks, especially in the initialisation times.

Based on the results from this research, it cannot be excluded that the use of additive manufacturing can be a useful tool to develop a phantom for proton therapy in lung tissue. However, it also cannot be said with certainty yet that it is possible, but still is a promising new manufacturing technique. To be able to decisively state that additive manufacturing will improve quality assurance in lung phantoms would require far more research into the nature of the interactions between protons and heterogeneous materials and the degeneration of the Bragg peak that this is associated with.

Recommendations

To be able to prove that additive manufacturing can be a useful tool in proton therapy, it might be interesting to broaden the scope of the research, since this research was mainly simulations, but also to perform more research on the parts that were mostly neglected in this research. For example, the performance of the Form2 was not properly verified, which is a possible 3D-printer that may be able to print at the desired level of detail. With the objects this would yield, it might also be interesting to irradiate them, in order to compare an actual irradiation to the simulations.

Furthermore, since the simulations performed on blocks with adjusted density show that it is possible to verify the proton range in porous material, if the Bragg peak is outside the adjusted density or porous segment. However, the question remains if this also holds for protons with a lower energy, thus those that will cause a Bragg peak inside the porous segment, such as the 80MeV proton beams in this research.

Also, these simulations have been performed on phantoms consisting solely of PVA, since this is a readily available printing material that has a fair analogy to human soft tissue, both based on their densities and on the composition. However, this may not be the most ideal material to represent lung tissue, other materials could be used to replace the PVA. Potential candidates are for instance polypropylene (PP), which is a commercially available printing material, or expanded polystyrene (EPS), even though this is not a commercially available printing material. However, a combination of manufacturing processes could be employed, which can be integrated into each other. As an example, the production process could be such that a hollow thorax is 3D-printed and filled with EPS.

What is more, there is the regularity of cylinder grid. This cause the dose distribution to also display this regularity. Therefore it may improve the results of the simulations if the porosity is achieved with true 3D structures, instead of the 2.5D structures that were used in this research. This will also benefit the results for Bragg peaks that are located inside the porous segment, which now also greatly reflect the regularity, especially in the fall-off.

Lastly, the phantom can be reversed, so that the protons first travel through some solid PVA before reaching the porous segment, which is in greater correspondence to actual lung irradiation. To make it even more anthropomorphic for a human thorax, inside the homogeneous PVA segment, some denser parts could be added to resemble the ribcage.

Acknowledgements

Of course, after having completed my thesis project, I realise that I could not have been able to do so without the help of the people around me, my family and friends. This list would be about half as long as the rest of the report if I were to mention you all by name, therefore I want to take the time to thank a few people in particular, who, in my opinion, have been of great help to me during my thesis.

First and foremost, I wish to thank my supervisor, Eelco Lens, for his unwavering and hearty support throughout this project. I am truly humbled by his help, patience and motivation, without which I could not have dreamt of completing the project anywhere near the shape it is in today.

Next, I want to thank Dennis Schaart and Eelco again, for the opportunity they presented me with when I came to them in search of a thesis project. With this I also have to thank Rogier, for drawing my attention to the MP&T research group and helping me get into contact with both Dennis and Eelco.

Furthermore, I must say that my rowing friends have been crucial to my thesis. Therefore I want to thank my crewmates, Rik, Bart and Bas, and my coaches, Tim and Stefan, for all the nice and exhausting training we did or you made us do and great competitions we rowed in, which helped me clear my head and to stay focused during this project. Next to my own crewmates, I want to thank the ladies and my fellow coaches of both the "*Natúúrlijk!*" and *"Strak"* crews, Anouk, Anne-Kee, Dévi, Ewout, Jasmijn, Lotte, Suzanne, Henk and Maaike, Charlotte, Esmee, Nadine, Saskia, and Willemijn, Alec, Fleur and Max, who I had the great fortune and pleasure of coaching and coaching with for multiple seasons, with which they provided the necessary distraction from my thesis work.

Lastly, I want to thank a group that is even larger than my rowing friends, thus is truly way too large to all mention individually by name, namely my fellow students and other members of the research groups MP&T and ARI, for all your good advice, nice coffee breaks and the general nice time you allowed me to have during the entirety of the project.

So, a warm and heartfelt thank you to all of you for your contribution to my thesis.

Thijs Moret,
Delft, August 2019.

References

[1] CBS, “Sterftecijfers: CBS voorlopige cijfers uit 2018,” IKNL, 2019.

[2] J. van den Eijnde and M. Schouwenburg, Praktische Stralingshygiëne, Utrecht: Syntax Media, 2013.

[3] A. J. J. Bos, F. S. Draaisma and W. J. C. Okx, Inleiding tot de Stralingshygiëne, Den Haag: SDU Uitgevers, 2007.

[4] R. R. Wilson, “Radiological use of fast protons,” *Radiology,* vol. 47, no. 5, pp. 487-491, 1946.

[5] H. Paganetti, “Range uncertainties in proton therapy and the role of Monte Carlo simulations,” *Physics in Medicine and Biology,* vol. 57, no. 11, pp. 99-117, 2012.

[6] K. Ilicic, S. E. Combs and T. E. Schmid, “New insights in the relative radiobiological effectiveness of proton irradiation,” *Radiation Oncology,* vol. 13, no. 1, 2018.

[7] J. M. Slater, J. O. Archambeau, D. W. Miller, M. I. Notarus, W. Preston and J. D. Slater, “The Proton treatment center at Loma Linda University Medical Center: Rationale for and description of its development,” *International Journal of Radiation Oncology, Biology, Physics,* vol. 22, no. 2, pp. 383-389, 1992.

[8] H. Paganetti, “Proton Therapy: History and Rationale,” in *Proton Therapy Physics*, Boca Raton, CRC Press, 2012, pp. 1-18.

[9] H. Paganetti, Proton Therapy Physics, Boca Raton: CRC Press, 2012.

[10] A. W. Chan and N. J. Liebsch, “Proton Radiation Therapy for Head and Neck Cancer,” *Journal of Surgical Oncology,* no. 97, pp. 697-700, 2008.

[11] T. Mitin and A. L. Zietman, “Promise and Pitfalls of Heavy-Particle Therapy,” *Journal of Clinical Oncology,* vol. 32, no. 26, pp. 2855-2863, 2014.

[12] L. A. DeWerd and M. Kissick, The Phantoms of Medical and Health Physics, New York: Springer, 2014.

[13] R. van Oossanen, “Development of a 3D-printed phantom for proton therapy,” Delft, 2017.

[14] L. Zuofeng, R. Slopsema, S. Flampouri and D. K. Yeung, “Quality Assurance and Commissioning,” in *Proton Therapy Physics*, Boca Raton, CRC Press, 2014, pp. 221-264.

[15] M. Vitale, M. Cotteleer and J. Holdowsky, “An overview of Additive Manufacturing,” *Defence AT&L,* November-December 2016.

[16] J. R. C. Dizon, A. H. Espera Jr., Q. Chen and R. C. Advincula, “Mechanical characterization of 3D-printed polymers,” *Additive Manufacturing,* no. 20, pp. 44-67, 2018.

[17] H. Miyanija, N. Momenzadeh and L. Yang, “Effect of printing speed on quality of printed parts in Binder Jetting Process,” *Additive Manufacturing,* no. 20, pp. 1-10, 2018.

[18] T. DebRoy, H. L. Wei, J. S. Zuback, T. Mukherjee, J. W. Elmer, J. O. Milewski, A. M. Beese, A. Wilson-Heid, A. De and W. Zhang, “Additive manufacturing of metallic components – Process, structure and properties,” *Progress in Materials Science,* no. 92, pp. 112-224, 2018.

[19] J. Wu, Z. Zhao, C. M. Hamel, X. Mu, X. Kuang, Z. Guo and H. Jerry Qi, “Evolution of material properties during free radical photopolymerization,” *Journal of the Mechanics and Physics of Solids,* no. 112, pp. 25-49, 2018.

[20] “Formlabs,” [Online]. Available: https://formlabs.com/3d-printers/form-3/tech-specs/. [Accessed 09 07 2019].

[21] J. Madamesila, P. McGeachy, J. Eduardo Villarreal Barajas and R. Khan, “Characterizing 3D printing in the fabrication of variable density phantoms for quality assurance of radiotherapy,” *Physica Medica,* no. 32, pp. 242-247, 2016.

[22] J. Perl, J. Shin, J. Schümann, B. Faddegon and H. Paganetti, “TOPAS: An innovative proton Monte Carlo platform for research,” *Medical Physics,* vol. 39, no. 11, pp. 6818-6837, 2012.

[23] S. Agostinelli, J. Allison, K. Amako, J. Apostolakis and H. Araujo, “Geant4 - A simulation toolkit,” *Nuclear Instruments and Methods in Physics Research A,* vol. 506, no. 3, pp. 250-303, 2003.

[24] J. Allison, K. Amako, J. Apostolakis, P. Arce, M. Asai, T. Aso, E. Bagli and A. Bagulya, “Recent developments in GEANT4,” *Nuclear Instruments and Methods in Physics Research A,* vol. 835, pp. 186-225, 2016.

[25] J. Meija, T. B. Coplen, M. Berglund, W. A. Brand, P. De Bièvre, M. Gröning, N. E. Holden, J. Irrgeher, R. D. Loss, T. Walczyk and T. Prohaska, “Atomic weights of the elements 2013 (IUPAC Technical Report),” *Pure and Applied Chemistry,* vol. 88, no. 3, pp. 265-291, 2016.

[26] A. Andrzejewska, “Biomechanical properties of 3D-printed bone models,” *BioSystems,* no. 176, pp. 52-55, 2019.

[27] A. A. Zadpoor, “Mechanical performance of additively manufactured meta-biomaterials,” *Acta Biomaterialia,* no. 85, pp. 41-59, 2019.

[28] U. K. Roopavath, S. Malferrari, A. van Haver, F. Verstreken, S. Narayan Rath and D. M. Kalaskar, “Optimization of extrusion based ceramic 3D printing process for complex bony designs,” *Materials and Design,* no. 162, pp. 263-270, 2019.

Appendices

Appendix A – Applicability of AM processes

The complete table of AM processes as individually discussed in AM processes in Table 1.

Table 10, Complete list of applicability of different AM processes

AM process	Materials	Print speed	Quality	Other
FDM – MJ	+	-	+	+/-
FDM – ME	+/-	-	+	+/-
PBF – L	+ +	+	+ +	+
PBF – EB	-	+	+	-
BJ	+	+	+/-	+/-
VPP – SLA	+	+ +	+ +	+
VPP – DLP	+	+ +	+	+
SL – LOM	+	- -	-	+/-
SL – UAM	+/-	- -	- -	+/-
DED – L	-	+	+/-	- -
DED - EB	-	+	+/-	- -

Appendix B – Example of TOPAS MC simulation

The following code is used to control the simulations in TOPAS MC. This specific simulation only shows the first even and odd layer cylindrical inserts, since the only difference there is with the subsequent layers is a change in the X and Y directional shift. If there is a pound sign preceding a line of code, this is not taken into account as TOPAS MC regards this as a comment. Thus, the example specified here has the graphics controls commented out, which is done to speed up the simulation process, as graphics display costs a lot of computational power.

```
##########################################
######## Control #######
##########################################
b:Sc/ScoringOn = "True"
b:Ts/DumpParameters = "True"
i:Ts/ShowHistoryCountAtInterval = 1000
b:Ts/ShowCPUTime = "True"
i:Ts/Seed = 1
i:Ts/MaxInterruptedHistories = 750
#b:Ts/PauseBeforeQuit = "True"
i:Ts/MaxStepNumber = 50000
##########################################
######## Graphics #########
##########################################
#s:Gr/ViewA/Type = "OpenGL"
#i:Gr/ViewA/WindowSizeX = 1800
#i:Gr/ViewA/WindowSizeY = 1000
#b:Gr/ViewA/IncludeAxes = "True"
#d:Gr/ViewA/AxesSize = 0.1 m
#d:Gr/ViewA/Theta = 45 deg
#d:Gr/ViewA/Phi = 45 deg
#s:Gr/ViewA/Projection = "Perspective"
#d:Gr/ViewA/PerspectiveAngle = 30 deg
#u:Gr/ViewA/Zoom = 1.5
#s:Gr/ViewA/RefreshEvery = "Session"
#s:Gr/ViewA/ColorBy = "ParticleType"
#sv:Gr/ViewA/ColorByParticleTypeNames = 4  "proton" "e-" "gamma" "neutron"
#sv:Gr/ViewA/ColorByParticleTypeColors = 4  "blue" "red" "yellow" "magenta"
##########################################
######## World ########
##########################################
b:Ge/World/Invisible = "True"
##########################################
######## Beam 1 ########
##########################################
s:Ge/BeamPosition1/Parent = "World"
s:Ge/BeamPosition1/Type = "Group"
d:Ge/BeamPosition1/TransX = -12.5 cm
d:Ge/BeamPosition1/TransY = 0 cm
d:Ge/BeamPosition1/TransZ = 0 cm
d:Ge/BeamPosition1/RotX = 0.000 deg
d:Ge/BeamPosition1/RotY = -90.000 deg
```

```
d:Ge/BeamPosition1/RotZ = 0.000 deg
s:So/Beam1/Type = "Beam"
s:So/Beam1/Component = "BeamPosition1"
s:So/Beam1/BeamParticle = "proton"
d:So/Beam1/BeamEnergy = 160.000 MeV
u:So/Beam1/BeamEnergySpread = 1.0
s:So/Beam1/BeamPositionDistribution = "Gaussian"
s:So/Beam1/BeamPositionCutoffShape = "Ellipse"
d:So/Beam1/BeamPositionCutoffX = 10 cm
d:So/Beam1/BeamPositionCutoffY = 10 cm
d:So/Beam1/BeamPositionSpreadX = 4.4548 mm
d:So/Beam1/BeamPositionSpreadY = 4.4548 mm
s:So/Beam1/BeamAngularDistribution = "Gaussian"
d:So/Beam1/BeamAngularCutoffX = 90. deg
d:So/Beam1/BeamAngularCutoffY = 90. deg
d:So/Beam1/BeamAngularSpreadX = 0.0032 rad
d:So/Beam1/BeamAngularSpreadY = 0.0032 rad
s:So/Beam1/BeamXYDistribution = "Gaussian"
d:So/Beam1/BeamStandardDeviationX = 0.0 cm
d:So/Beam1/BeamStandardDeviationY = 0.0 cm
i:So/Beam1/NumberOfHistoriesInRun = 1500000
#########################################
######## Scorer ########
#########################################
s:Ge/Scoring3D/Parent = "World"
s:Ge/Scoring3D/Type = "TsBox"
b:Ge/Scoring3D/IsParallel = "True"
s:Ge/Scoring3D/ParallelWorldName = "3DScoringWorld"
d:Ge/Scoring3D/HLX = 125.00 mm
d:Ge/Scoring3D/HLY = 50.00 mm
d:Ge/Scoring3D/HLZ = 50.00 mm
d:Ge/Scoring3D/TransX = 0 cm
d:Ge/Scoring3D/TransY = 0 cm
d:Ge/Scoring3D/TransZ = 0 cm
d:Ge/Scoring3D/RotX = 0 deg
d:Ge/Scoring3D/RotY = 0 deg
d:Ge/Scoring3D/RotZ = 0 deg
b:Sc/Scoring3D/Invisible = "True"
s:Sc/ScoreBox3D/Quantity = "DoseToMedium"
s:Sc/ScoreBox3D/Component = "Scoring3D"
i:Sc/ScoreBox3D/XBins = 500
i:Sc/ScoreBox3D/YBins = 200
i:Sc/ScoreBox3D/ZBins = 200
s:Sc/ScoreBox3D/OutputType = "CSV"
s:Sc/ScoreBox3D/OutputFile = "CB_Block_Circles_Virt_v8_qubic_vox_DTM_Thijs"
s:Sc/ScoreBox3D/IfOutputFileAlreadyExists = "increment"
b:Sc/ScoreBox3D/OutputToConsole = "False"
b:Sc/ScoreBox3D/Active = "True"
s:Sc/ScoreBox3Doption2/Quantity = "DoseToWater"
s:Sc/ScoreBox3Doption2/Component = "Scoring3D"
i:Sc/ScoreBox3Doption2/XBins = 500
i:Sc/ScoreBox3Doption2/YBins = 200
i:Sc/ScoreBox3Doption2/ZBins = 200
s:Sc/ScoreBox3Doption2/OutputType = "CSV"
s:Sc/ScoreBox3Doption2/OutputFile = "CB_Block_Circles_Virt_v8_qubic_vox_DTW_Thijs"
```

```
s:Sc/ScoreBox3Doption2/IfOutputFileAlreadyExists = "increment"
b:Sc/ScoreBox3Doption2/OutputToConsole = "False"
b:Sc/ScoreBox3Doption2/Active = "True"
##########################################
######## Block ########
##########################################
s:Ge/Block/Parent = "World"
s:Ge/Block/Type = "TsBox"
s:Ge/Block/Material = "G4_POLYVINYL_ALCOHOL"
d:Ge/Block/HLX = 125.00 mm
d:Ge/Block/HLY = 50.00 mm
d:Ge/Block/HLZ = 50.00 mm
s:Ge/Block/Color = "Lightblue"
s:Ge/Block/DrawingStyle = "WireFrame"
##########################################
######## Odd Layer 01, Insert 01 ########
##########################################
s:Ge/ODDInsert0101/Parent = "Block"
s:Ge/ODDInsert0101/Type = "TsCylinder"
s:Ge/ODDInsert0101/Material = "Air"
d:Ge/ODDInsert0101/RMin = 0 mm
d:Ge/ODDInsert0101/RMax = 0.500 mm
d:Ge/ODDInsert0101/HL = 50.000 mm
d:Ge/ODDInsert0101/SPhi = 0 deg
d:Ge/ODDInsert0101/DPhi = 360 deg
d:Ge/ODDInsert0101/TransZ = 0 mm
d:Ge/ODDInsert0101/TransY = -49.00 mm
d:Ge/ODDInsert0101/TransX = -115.00 mm
s:Ge/ODDInsert0101/Color = "White"
s:Ge/ODDInsert0101/DrawingStyle = "Solid"
##########################################
######## Even Layer 01, Insert 01 ########
##########################################
s:Ge/EVENInsert0101/Parent = "Block"
s:Ge/EVENInsert0101/Type = "TsCylinder"
s:Ge/EVENInsert0101/Material = "Air"
d:Ge/EVENInsert0101/RMin = 0 mm
d:Ge/EVENInsert0101/RMax = 1.500 mm
d:Ge/EVENInsert0101/HL = 50.000 mm
d:Ge/EVENInsert0101/SPhi = 0 deg
d:Ge/EVENInsert0101/DPhi = 360 deg
d:Ge/EVENInsert0101/TransY = -44.75 mm
d:Ge/EVENInsert0101/TransX = -112.00 mm
d:Ge/EVENInsert0101/TransZ = 0 mm
s:Ge/EVENInsert0101/Color = "Red"
s:Ge/EVENInsert0101/DrawingStyle = "Solid"
##########################################
```